OPEN ACCESS



The Scatter Matters: Circumgalactic Metal Content in the Context of the M- σ Relation

N. Nicole Sanchez 1,2,3,11 , Jessica K. Werk 0, Charlotte Christensen 0, O. Grace Telford 1,5,6 , Thomas R. Quinn 0, Michael Tremmel 7,8 , Jennifer Mead 0, Ray S. Sharma 0, and Alyson M. Brooks 6,10 , and Alyson M. Brooks 6,10 , and Carrengie Institution for Science, 813 Santa Barbara Street, Pasadena, CA 91101, USA; nsanchez@carnegiescience.edu 2 Cahill Center for Astronomy and Astrophysics, California Institute of Technology, MC249-17, Pasadena, CA 91125, USA 3 Astronomy Department, University of Washington, Seattle, WA 98195, USA 4 Physics Department, Grinnell College, 1116 Eighth Avenue, Grinnell, IA 50112, USA 5 Department of Astrophysical Sciences, Princeton University, 4 Ivy Lane, Princeton, NJ 08544, USA 6 Rutgers University, Department of Physics and Astronomy, 136 Frelinghuysen Road, Piscataway, NJ 08854, USA 7 Astronomy Department, Yale University, P.O. Box 208120, New Haven, CT 06520, USA 8 School of Physics, University College Cork, College Road, Cork, T12 K8AF, Ireland 9 Columbia University, Department of Astronomy, New York, NY 10025, USA 10 Center for Computational Astrophysics, Flatiron Institute, 162 5th Avenue, New York, NY 10010, USA Received 2023 April 13; revised 2024 March 22; accepted 2024 April 1; published 2024 May 22

Abstract

The interaction between supermassive black hole (SMBH) feedback and the circumgalactic medium (CGM) continues to be an open question in galaxy evolution. In our study, we use smoothed particle hydrodynamics simulations to explore the impact of SMBH feedback on galactic metal retention and the motion of metals and gas into and through the CGM of L* galaxies. We examine 140 galaxies from the 25 Mpc cosmological volume ROMULUS25, with stellar masses between $\log(M_*/M_\odot) = 9.5-11.5$. We measure the fraction of metals remaining in the interstellar medium (ISM) and CGM of each galaxy and calculate the expected mass of each SMBH based on the $M_{\rm BH}-\sigma$ relation (Kormendy & Ho 2013). The deviation of each SMBH from its expected mass, $\Delta M_{\rm BH}$, is compared to the potential of its host via σ . We find that SMBHs with accreted mass above $M_{\rm BH}-\sigma$ are more effective at removing metals from the ISM than undermassive SMBHs in star-forming galaxies. Overall, overmassive SMBHs suppress the total star formation of their host galaxies and more effectively move metals from the ISM into the CGM. However, we see little to no evacuation of gas from the CGM out of their halos, in contrast with other simulations. Finally, we predict that C IV column densities in the CGM of L* galaxies are unlikely to depend on host galaxy SMBH mass. Our results show that the scatter in the low-mass end of the $M_{\rm BH}-\sigma$ relation may indicate how effective an SMBH is in the local redistribution of mass in its host galaxy.

Unified Astronomy Thesaurus concepts: Galaxy evolution (594); N-body simulations (1083); Hydrodynamical simulations (767); M-sigma relation (2026); Milky Way mass (1058); Circumgalactic medium (1879); Galaxy chemical evolution (580); Supermassive black holes (1663); Active galactic nuclei (16)

1. Introduction

The vastly different scales between the event horizon of a supermassive black hole (SMBH) and the size of its host galaxy have been evocatively described by Savorgnan & Graham (2016) as the difference between a grain of sand and the entirety of the Saharan Desert (a difference of approximately 10 orders of magnitude). While the size difference between these objects makes their interaction puzzling, mounting evidence continues to connect the evolution and properties of galaxy hosts to their SMBHs (Haehnelt et al. 1998; Magorrian et al. 1998; Ferrarese & Merritt 2000; Gebhardt et al. 2000; Reines & Volonteri 2015; Saglia et al. 2016).

The relation between the mass of the central SMBH, $M_{\rm BH}$, and the stellar dispersion of its host galaxy's bulge, σ_* , is one of the most fundamental relations drawn between the SMBH and its host galaxy (Kormendy & Ho 2013 and citations therein). Colloquially known as the $M_{\rm BH}$ – σ relation, this

Original content from this work may be used under the terms of the Creative Commons Attribution 4.0 licence. Any further distribution of this work must maintain attribution to the author(s) and the title of the work, journal citation and DOI.

observed relation shows a tight correlation across 3 orders of magnitude in SMBH mass and is theorized to tie together the growth of an SMBH—during its tenure as an active galactic nucleus (AGN)—and the winds launched from its accretion disk. These winds are responsible for removing some of the gas necessary for continued star formation in the galaxy. In this way, the energetics of the SMBH work to regulate the star formation in the bulge of massive galaxies. When the SMBH is no longer accreting or driving outflows, gas accretion and star formation can resume (Alexander et al. 2005; Papovich et al. 2006; Volonteri 2012). The quantity σ_* not only reflects the mass of its host galaxy, but also approximates the depth of the galaxy's potential well (Ferrarese & Merritt 2000; Zahid et al. 2018; Ricarte et al. 2019).

The scatter in the $M_{\rm BH}$ – σ relation can further illuminate the processes that drive galaxy evolution at all galaxy masses. At the high-mass end, there is less scatter and observations at this scale are dominated by more massive BHs residing in massive ellipticals above $\sim 10^{13}~M_{\odot}$ (Van Den Bosch et al. 2007; Moster et al. 2010; Emsellem et al. 2011; Natarajan 2011; Dubois et al. 2015). However, lower-mass BHs live in a more diverse range of galaxy masses, resulting in scatter that is more pronounced on the low-mass end of the relation. This low-mass-end scatter may be explained by the variable pathways that drive SMBH growth (Micic et al. 2007; Volonteri &

¹¹ NSF MPS-Ascend Fellow.

Natarajan 2009; Reines et al. 2013; Graham & Scott 2015; Sharma et al. 2020). Galaxy mergers are thought to fuel SMBHs, in addition to building up galaxies and contributing to the assembly of bulges (Di Matteo et al. 2005; Shen et al. 2008; Sanchez et al. 2018). Furthermore, episodes of gas funneling into SMBHs result in feedback that removes gas from the galaxy, suppressing both continued SMBH growth and future star formation (Schawinski et al. 2010; Pontzen et al. 2017; Sanchez et al. 2021). A concerted effort has been put forth to explain the physical processes that result in the scatter on the $M_{\rm BH}-\sigma$ relation. However, the impact on galaxy properties by SMBHs that deviate from the $M_{\rm BH}-\sigma$ relation has not been well constrained, especially within the context of the circumgalactic medium (CGM).

The rise of observational surveys of the CGM with the Cosmic Origins Spectrograph (COS) on the Hubble Space Telescope (HST) has inspired a range of theoretical studies focused on the connection between feedback processes and the content of the CGM. Simulations were initially hard-pressed to match the observational survey results carried out with the COS (e.g., Tumlinson et al. 2013; Werk et al. 2013). Predictions for column densities of high ions like O VI were too low, and low-ion column densities were difficult to replicate in the simulated environments of cosmological volumes (Oppenheimer et al. 2016; Suresh et al. 2017).

More recently, cosmological simulations have updated the subgrid prescriptions in their codes to better characterize the low-density, multiphase medium of the CGM (Shen et al. 2012; Stinson et al. 2012; Vogelsberger et al. 2014; Schaye et al. 2015; Tremmel et al. 2017); furthermore, recent work has focused on connecting the impact of energetic feedback from a galaxy's SMBH to the diffuse CGM. Broadly, simulations have shown that the SMBH can impact the CGM in a multitude of ways: heating and evacuating (or removing) gas in the disk to quench star formation in the galaxy (IllustrisTNG and EAGLE simulations; Oppenheimer et al. 2016; Suresh et al. 2017; Nelson et al. 2018), driving metal-rich gas out of galaxy centers and moving metal-rich gas into (enriching) the CGM (IllustrisTNG and ROMULUS25, or R25; Nelson et al. 2019; Sanchez et al. 2019), as well as ejecting CGM gas out into the intergalactic medium (IGM; EAGLE; Oppenheimer et al. 2018). Furthermore, Mitchell et al. (2020) find that more gas flows out of the halo virial radius than from the interstellar medium (ISM) of central galaxies in the EAGLE simulations, implying increased mass loading within the CGM, while CGM mass fractions decline after explosive episodes of AGN-driven feedback in galaxies from both EAGLE and IllustrisTNG (Oppenheimer et al. 2020a). At lower masses, Sharma et al. (2022) show that though SMBHs can drive outflows in some dwarf galaxies in R25, gas does not often leave the CGM.

Overall, these cosmological simulations seem to paint a similar picture. Both the EAGLE and Illustris/IllustrisTNG simulations predict the evacuation of the CGM in the massive galaxies where SMBH processes dominate. However, this may not be the whole story. Chadayammuri et al. (2022) compare CGM radial profiles from eROSITA and mock X-ray observations from the IllustrisTNG and EAGLE cosmological simulations. They find that the luminosity of the CGM of their observed galaxies is higher than that predicted by the simulations, indicating that more explosive AGN feedback prescriptions may over-evacuate the CGM of their galaxies.

Furthermore, recent work from Davies et al. (2020) ties the expulsion of gas by SMBH-driven outflows to the scatter in the halo gas fraction at fixed M_{200} in both the IllustrisTNG and EAGLE simulations. Galaxies with more massive BHs (within a fixed-halo-mass bin) reside within more gas-poor halos, while galaxies with undermassive BHs retain a higher gas fraction in the CGM as well as show elevated star formation rates (SFRs). Davies et al. (2020) find that the evacuation of CGM gas by SMBH feedback is a critical step in the morphological evolution and quenching of their galaxies. These results point to an intrinsic connection between BH masses and the evolution of the CGM. We follow this line of investigation to further our understanding of how the deviation of an SMBH's mass from empirical expectations impacts its host halo gas.

In this paper, we examine how deviation in SMBH mass from the empirical $M_{\rm BH}$ – σ relation changes the overall effectiveness of SMBH feedback at moving gas and driving metal flows into and out of the CGM. We explore this change across 2 orders of magnitude in stellar mass, 9.5 < log (M_*/M_\odot) < 11.5. Our study includes comparisons between the R25 simulations and observational constraints, such as metal retention fractions, and makes predictions for ion column density measurements in the CGM of galaxies with dynamically measured SMBH mass measurements.

This paper is organized as follows. Section 2 introduces our simulations and the galaxy selection process, and in Section 3 we describe and analyze our results. In Section 4, we compare our findings to observed measurements from the literature as well as a set of mock observational data and discuss the broader context for our results and their implications.

2. Simulated Galaxy Sample

2.1. Simulation Parameters

All of the galaxies examined in this paper were selected from the R25 simulation (Tremmel et al. 2017; Ricarte et al. 2019; Sharma et al. 2020), a 25 Mpc cosmological volume, run with the smoothed particle hydrodynamics (SPH) N-body tree code, Charm N-body Gravity solver (ChaNGa; Menon et al. 2015). ChaNGa adopts its models for cosmic UV background, star formation based on a Kroupa initial mass function (IMF), and "blastwave" supernova (SN) feedback from the well-tested GASOLINE code (Wadsley et al. 2004, 2008; Stinson et al. 2006; Shen et al. 2010). Rates from Type Ia and Type II SNe are implemented through the Raiteri et al. (1996) method, using the stellar lifetime calculations of the Padova group for stars with varying metallicities (Alongi et al. 1993; Bressan et al. 1993; Bertelli et al. 1994). We use the following parameters for our stellar subgrid models: star-forming efficiency, $c_* = 0.15$; the fraction of SN energy that couples to the ISM, $\epsilon_{SN} = 0.75$; and the amount of SN energy imparted to the gas is 10⁵¹ erg. For additional details about the SN "blastwave" radius and SNe Ia and II metal enrichment prescriptions, see Stinson et al. (2006).

ChaNGa includes an SPH formalism that updates the force expression to include a geometric averaged density approach (Wadsley et al. 2017). This hydrodynamics treatment includes thermal and metal diffusion (Shen et al. 2010) and reduces artificial surface tension, to result in the improved resolution of fluid instabilities (Ritchie & Thomas 2001; Menon et al. 2015).

Gas cooling in R25 is regulated by metal abundance, as in Guedes et al. (2011); however, it does not include a full treatment of metal cooling. We include a low-temperature extension to the cooling curve that allows gas below 10⁴ K to cool proportionally to the metals in the gas. Gas above 10⁴ K cools only by H/He, Bremsstrahlung, and inverse Compton effects (see Tremmel et al. 2017 for full details).

Shen et al. (2012) compare simulations of Milky Way–mass halos at high redshift, finding that with realistic treatments of metal diffusion and stellar IMF, the inclusion of metal-line cooling does not influence the total stellar mass of the galaxy. In other cases, particularly at lower masses, the inclusion of metal-line cooling with the simplistic treatment of star formation at low resolution results in overcooling, requiring artificially strong feedback to overcome (Christensen et al. 2014). However, it cannot be overlooked that the inclusion of high-temperature metal-line cooling can influence the rate at which gas cools out of the CGM onto galaxies (van de Voort et al. 2011). At the metallicities (\sim 10%–30% Z_{\odot}) that we expect for the CGM of the most massive halos we study in this work, the lack of metal-line cooling will likely impact the cooling rates by a typical factor of 3-5 at the peak of the cooling curve at 10^{5.5-6} K when the effect of the UV background is accounted for Shen et al. (2010). The effect is nontrivial and this does represent a significant caveat to this work that we discuss further in Section 4.1.

R25 includes updated BH formation, accretion, and feedback prescriptions. BH formation ties seeds to dense and extremely low-metallicity gas to more effectively estimate SMBH populations in a variety of galaxy mass regimes. The SMBH accretion model is based on Bondi–Hoyle, but includes a consideration for angular momentum support from nearby gas. This update allows for more physically motivated growth than Bondi–Hoyle alone (Rosas-Guevara et al. 2016; Anglés-Alcázar et al. 2017). BHs form with the relatively high seed mass of $M_{\rm BH}=10^6~M_{\odot}$ to account for rapid early growth driven by environment and physical processes below the simulation resolution limit (Hosokawa et al. 2013; Schleicher et al. 2013).

Thermal SMBH feedback imparts energy on the nearest 32 gas particles according to kernel smoothing and is based on accreted mass, \dot{M} , via

$$E_{\rm BH} = \epsilon_r \epsilon_f \dot{M} c^2 dt, \tag{1}$$

where $e_f = 0.02$ and $e_r = 0.1$ are the feedback and radiative efficiency, respectively. Accretion is assumed to be constant for one BH time step, dt. This SMBH feedback prescription has been shown to successfully produce large-scale outflows (Pontzen et al. 2017; Tremmel et al. 2019). Finally, an updated dynamical friction prescription has been included to better track SMBH growth and dynamical evolution (Tremmel et al. 2015). For additional details about the BH prescriptions, see Tremmel et al. (2017).

R25 was run with a Λ CDM cosmology with $\Omega_0 = 0.3086$, $\Lambda = 0.6914$, h = 0.67, and $\sigma_8 = 0.77$ (Planck Collaboration 2016). R25 has a Plummer-equivalent force softening length of 250 pc and has a UV background through the evolution to z = 0 (Haardt & Madau 2012). R25 uses gas and DM particle resolutions of $3.4 \times 10^5~M_{\odot}$ and $2.1 \times 10^5~M_{\odot}$, respectively. Additionally, R25 has been optimized to match the observed stellar mass-halo mass relation of Moster et al. (2013)

and the SMBH-stellar mass relation using stellar mass and halo mass corrections from (Munshi et al. 2013).

2.2. Isolated Galaxies with
$$M_* = 10^{9.5-11.5} M_{\odot}$$

For comparison with observations, we select our sample of galaxies using a roughly L* stellar mass range that has been well inspected by observations (Tripp et al. 2011; Tumlinson et al. 2013; Werk et al. 2013; Borthakur et al. 2015; Wilde et al. 2021): $3 \times 10^9 \, M_\odot < M_* < 3 \times 10^{11} \, M_\odot$. Within R25, there are 282 galaxies within this stellar mass range at $z \sim 0$. We further refine our selection to remove galaxies that we consider satellites. We define satellites as galaxies within 300 kpc of another more massive galaxy. Using this definition, our main sample consists of 140 galaxies that host SMBHs at their centers. There are 119 star-forming (SF; specific SFR or sSFR $> 1.6 \times 10^{-11} \, M_\odot \, \text{yr}^{-1}$) galaxies in our sample and 21 are quenched (Q; sSFR $< 1.6 \times 10^{-11} \, M_\odot \, \text{yr}^{-1}$) at $z \sim 0$. In addition, we find 20 isolated galaxies within this mass range that do not host an SMBH at their center.

Figure 1 shows the $M_{\rm BH}$ – σ relation (Kormendy & Ho 2013) alongside measurements for our full sample of 140 galaxies with central SMBHs using the accreted SMBH mass ($M_{\rm BH,acc}$; left) and total SMBH mass ($M_{\rm BH,total}$; right). We find that both mass measurements for our sample fall along the line produced using the empirical $M_{\rm BH}$ – σ equation of Kormendy & Ho (2013):

$$\frac{M_{\rm BH,acc}}{10^9 M_{\odot}} = (0.309) \left(\frac{\sigma}{200 \text{ km s}^{-1}}\right)^{4.38},\tag{2}$$

where $M_{\rm BH,acc}$ represents the mass accreted by the SMBH (as in the left panel of Figure 1) and σ is the isolated stellar velocity dispersion of a central bulge, if one exists. We define $M_{\rm BH,acc}$ as the contribution of the SMBH mass obtained only by gas accretion, not including BH–BH mergers. We choose to use $M_{\rm BH,acc}$ throughout our analysis to conservatively account for the impact of our large BH seeds at the low-mass end of the relation, and we note that our main results remain unchanged despite this choice (Figure 2).

Meanwhile, we calculate the velocity dispersion of each galaxy, σ , as in Ricarte et al. (2019). We select the stellar bulge using a single Sérsic profile for each galaxy, with an assumed surface brightness cutoff of 32 mag arcsec⁻² and a maximum radius of $5R_{\text{half-light}}$. Then we calculate σ from the stars in this selected region using

$$\sigma = \sqrt{\langle v^2 \rangle - \langle v \rangle^2}, \tag{3}$$

where v is the 3D velocity of each particle (see Ricarte et al. 2019 for further details).

As in Ricarte et al. (2019), the fact that our galaxies mostly lie along the empirical $M_{\rm BH}$ – σ relation indicates that their growth is consistent with the observed phenomenon that SMBHs grow alongside the stellar content of their host galaxies. We refer the reader to Ricarte et al. (2019) for further details on the dominant physical processes driving the scatter in the low-mass end of the $M_{\rm BH}$ – σ relation in R25.

3. Results

The expulsion of metal-rich gas from the center of the galaxy by AGN feedback has recently been shown to be a key process for enriching the CGM (Nelson et al. 2019; Sanchez et al.

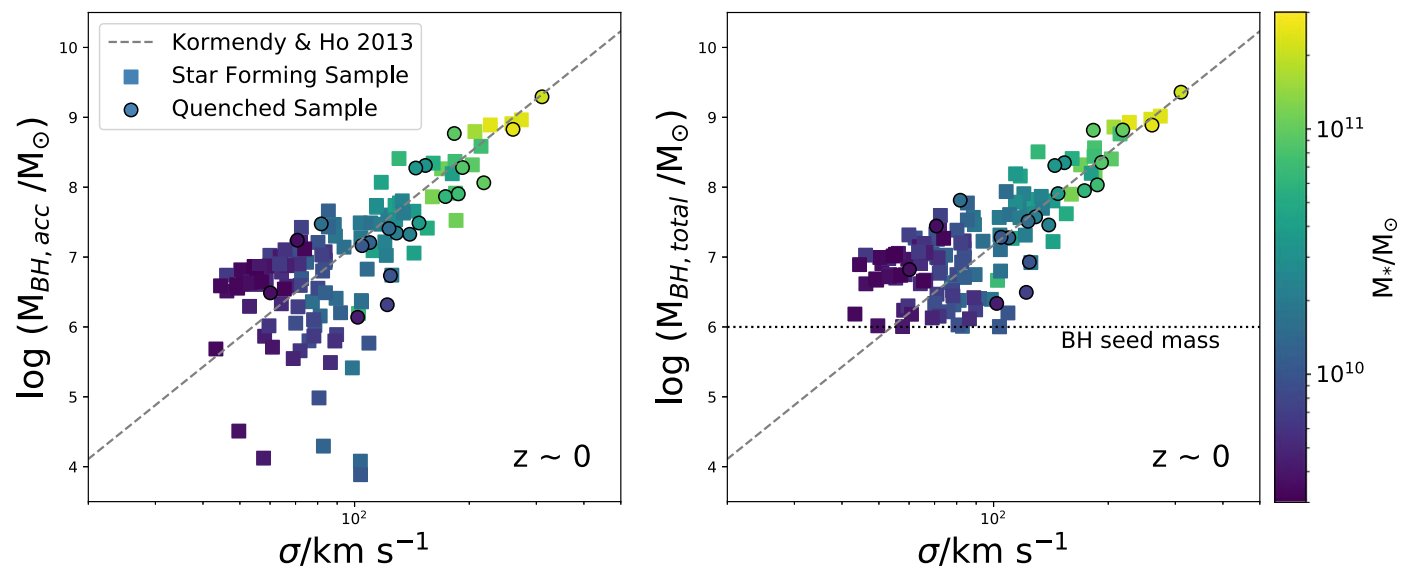


Figure 1. The $M_{\rm BH}-\sigma$ relation for the 140 galaxies within R25 that are within our selected stellar mass range and that contain an SMBH. Left: $M_{\rm BH}-\sigma$ relation using $M_{\rm BH,acc}$, the accreted mass for each SMBH, which neglects the large starting seed masses of $10^6 M_{\odot}$. Right: $M_{\rm BH}-\sigma$ relation using $M_{\rm BH,total}$, the total mass for each SMBH at z=0. In both plots, SF galaxies are denoted by squares and Q galaxies (sSFR $< 1.6 \times 10^{-11} M_{\odot} \ \rm yr^{-1}$) are shown as circles. The points are colored by the stellar mass of the galaxy. The spread of the galaxies falls along the $M_{\rm BH}-\sigma$ relation, the gray dashed line, of Kormendy & Ho (2013), though we note that at the lower-mass end, our sample tends to lie slightly above the line. By comparing these plots, we see that our choice to use $M_{\rm BH,acc}$ throughout the rest of the paper means that our BH masses are still well correlated with the empirical $M_{\rm BH}-\sigma$ relation, while accounting for the contribution of the large seed mass at the low-mass end of the relation.

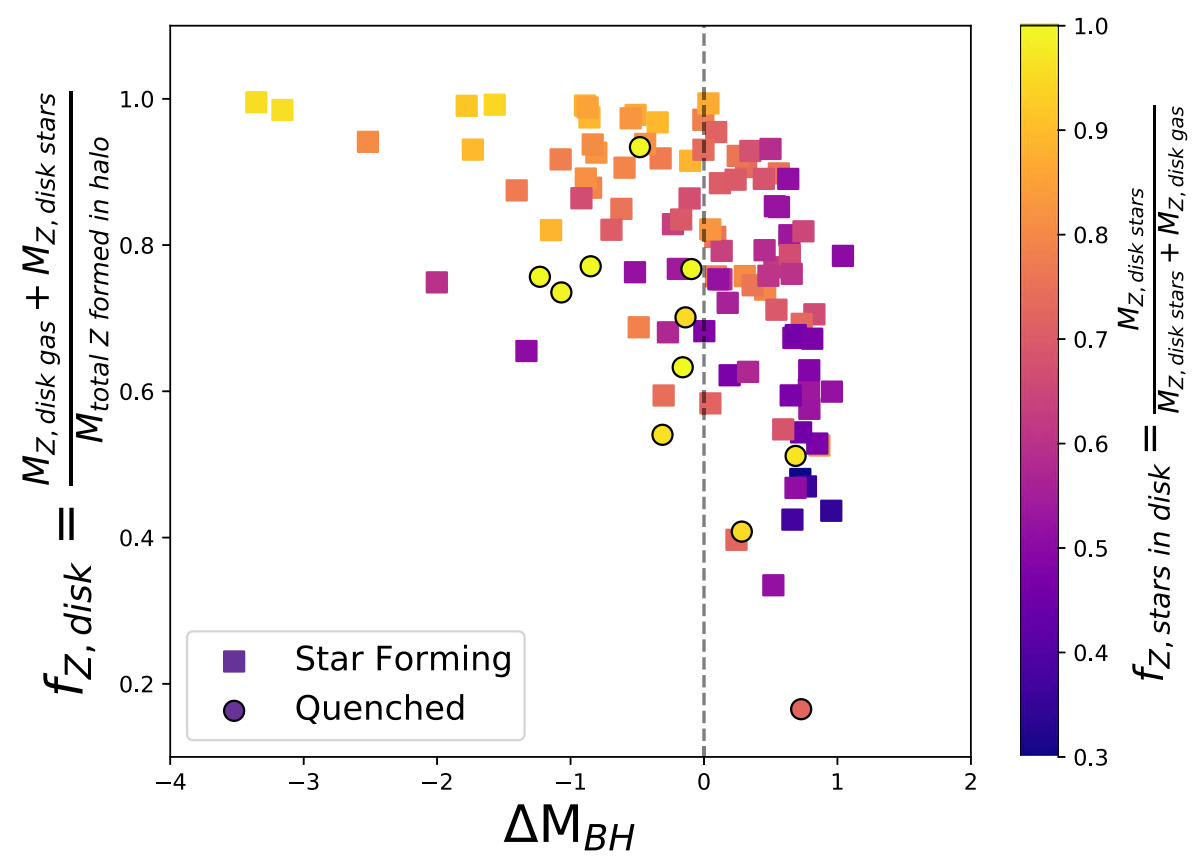


Figure 2. The metal retention in the disk, $f_{Z,disk}$, of our sample of galaxies from R25 as a function of ΔM_{BH} . The points are colored by the fraction of total disk metals contained in stars. SMBHs that are left of the gray line are undermassive compared to their host galaxy's stellar population (BH masses below the M_{BH} - σ relation; Figure 1, left panel) and maintain more of their metals in their disks or central regions. Meanwhile, galaxies to the right of the line are more effective at removing metals from the disk, with a similar effect seen in quiescent galaxies (circles).

2019). We continue this line of research to determine whether properties of the galaxy or the SMBH may impact this effect. To do this, we explore the galaxies from R25 and determine

where the metals in each galaxy remain. We split each galaxy into two main components. First, we define the "disk" or "central region" as the inner $0.1R_{\rm vir}$ of the galaxy, a

 Table 1

 Median Metal Retention Values from the R25 Samples at $z \sim 0$

Sample	No. of Galaxies	$f_{Z,\mathrm{halo}} \pm 1\sigma$	$f_{ m Z,disk} \pm 1\sigma$	$f_{\rm Z,CGM} \pm 1\sigma$
SF Overmassive SMBH	76	0.95 (±0.08)	0.73 (±0.15)	0.21 (±0.11)
SF Undermassive SMBH	42	$0.99~(\pm 0.02)$	$0.89 (\pm 0.16)$	$0.09 (\pm 0.15)$
Q Overmassive SMBH	9	$0.85~(\pm 0.14)$	$0.51~(\pm 0.15)$	$0.34~(\pm 0.13)$
Q Undermassive SMBH	12	$0.86~(\pm 0.10)$	$0.72~(\pm 0.09)$	$0.13 \ (\pm 0.13)$
Q (All)	21	$0.85~(\pm 0.12)$	$0.63~(\pm 0.16)$	$0.26~(\pm 0.15)$
$M_* > 10^{10} M_{\odot}$	76	$0.97~(\pm 0.07)$	$0.76~(\pm 0.17)$	$0.16 \ (\pm 0.15)$
$M_* < 10^{10} M_{\odot}$	64	$0.96~(\pm 0.11)$	$0.75~(\pm 0.17)$	$0.20 \ (\pm 0.11)$
$M_{\rm SMBH} > 10^{7.6} M_{\odot}$	41	$0.95~(\pm 0.05)$	$0.66~(\pm 0.13)$	$0.29~(\pm 0.12)$
$M_{\rm SMBH} < 10^{7.6} M_{\odot}$	99	$0.97~(\pm 0.10)$	$0.77~(\pm 0.18)$	$0.15~(\pm 0.13)$

conventional definition of the galaxy–CGM boundary (Sales et al. 2009; Howk et al. 2017). Then, the CGM is defined to include all particles from $0.1R_{\rm vir}$ extending out to the virial radius.

We define the metal retention fraction as the fraction of total metals retained by each component within individual galaxies. For example, the metal retention fraction of the disk/central region component is calculated using the formula from Telford et al. (2019):

$$f_{Z,\text{disk}} = \frac{M_{Z,\text{disk gas,present}} + M_{Z,\text{disk *,present}}}{M_{Z,\text{formed}}},$$
 (4)

where $M_{Z,\text{disk gas,present}}$ and $M_{Z,\text{disk *,present}}$ are the amounts of mass contained in metals in gas and stars, respectively, within the central region at z=0. Similarly, the comparable fractions for the metals in the CGM are calculated as

$$f_{Z,CGM} = \frac{M_{Z,CGM \text{ gas,present}} + M_{Z,CGM *,present}}{M_{Z,formed}},$$
 (5)

where $M_{Z,{\rm CGM~gas,present}}$ and $M_{Z,{\rm CGM~*,present}}$ are the amounts of mass contained in the metals in gas and stars, respectively, within the region between $0.1R_{\rm vir}$ and $R_{\rm vir}$ also at z=0.

In both functions above, $M_{Z, \text{formed}}$ indicates the amount of metals formed throughout the simulation by stars that reside within the halo at z=0. To calculate this value, we duplicate the calculations done by the simulation using PYNBODY (Pontzen et al. 2013) and determine the metal yields from SNe Ia and SNe II for all of the star particles in the halo at z=0.

We calculate $M_{\rm BH,exp}$, the expected SMBH mass for a galaxy's velocity dispersion, using Equation (2) above (Kormendy & Ho 2013). From this value, we define the deviation from $M_{\rm BH,exp}$ as

$$\Delta M_{\rm BH} = \log_{10}(M_{\rm BH,acc}) - \log_{10}(M_{\rm BH,exp}),$$
 (6)

where $M_{\rm BH,acc}$ is measured from the simulation and is shown on the y-axis of Figure 1.

From the $\Delta M_{\rm BH}$, we further classify our sample into two sets: galaxies with overmassive SMBHs and galaxies with undermassive SMBHs. Galaxies in the first set, those with overmassive SMBHs compared to their $M_{\rm BH,exp}$, have a positive deviation, $\Delta M_{\rm BH} > 0$, and fall above the gray line in Figure 1. Galaxies with undermassive SMBHs fall below the empirical $M_{\rm BH} - \sigma$ line and have a negative $\Delta M_{\rm BH}$. We note that in our sample, low-stellar-mass galaxies are more likely to host overmassive BHs. Finally, where applicable, we include the galaxies without central SMBHs for additional comparison.

3.1. Scatter in the Low-mass End of M_{BH} - σ

In Figure 1, we see that scatter, and therefore $\Delta M_{\rm BH}$, is greatest at the low-mass end of the relation, as expected by both observations and simulations (Kormendy & Ho 2013; Habouzit et al. 2021). To address the enhanced scatter at the low-mass end and remove the impact of galaxy mass from our results, we focus this section of our analysis on galaxies in the lower half of our sample with stellar masses below $3\times 10^{10}M_{\odot}$. Our low-mass sample includes 106 galaxies from our full sample of 140 galaxies, with 95 SF and 11 Q galaxies. All of our galaxies without central SMBHs also fall inside this mass range.

3.1.1. Metal Retention Correlates with ΔM_{BH}

In Figure 2, we find that the metal retention in the disk correlates with the deviation of each galaxy's central SMBH from their $M_{\rm BH,exp}$, $\Delta M_{\rm BH}$. Galaxies with overmassive SMBHs can retain significantly less metals within their disks, with SF galaxies showing a median of $f_{Z,\rm disk}=0.73$ of their metals from the disk and Q galaxies a median of 0.51 (Table 1). Galaxies with undermassive BHs retain most, if not all, of their metals within the disk, with medians of $f_{Z,\rm disk}$ of 0.89 and 0.72 for SF and Q galaxies, respectively. We also find that most of the metals that remain in the disks or central regions of the galaxies with undermassive BHs are locked in stars (yellow points). Meanwhile, galaxies with overmassive SMBHs have a majority of their metals stored in the gas phase (purple points).

We can determine where the metals lost by each galaxy end up from Figure 3, which compares the total metals retained in the entire halo $(f_{Z,\mathrm{disk}}+f_{Z,\mathrm{cgm}})$ as a function of halo mass. Each point is colored by the metal mass fraction of the disk/central region in stars, as calculated by

$$f_{Z,\text{stars in disk}} = \frac{M_{Z,\text{disk stars}}}{M_{Z,\text{disk stars}} + M_{Z,\text{disk gas}}},$$
 (7)

where each value is calculated as described in Section 2.

We find that the majority of our SF galaxies keep nearly all of their metals within the halo, with only up to 15% of their metals being lost to the IGM. Only $\sim 5\%$ (6/119) of these SF galaxies lose more than 15% of their metals to the IGM (indicated by the dashed gray line at y=0.85). Furthermore, by comparing the color of the points, we can see that in the SF galaxies that keep most of their metals, those metals are primarily stored in stars within the disk (yellow-to-orange squares). The SF galaxies that lose more of their metals to the CGM (purple squares) have more of the metals in their disk contained within the gas phase. The metal retention history of SF galaxies is likely impacted by their SMBHs. In the SF galaxies with overmassive BHs, the SMBH may not only be

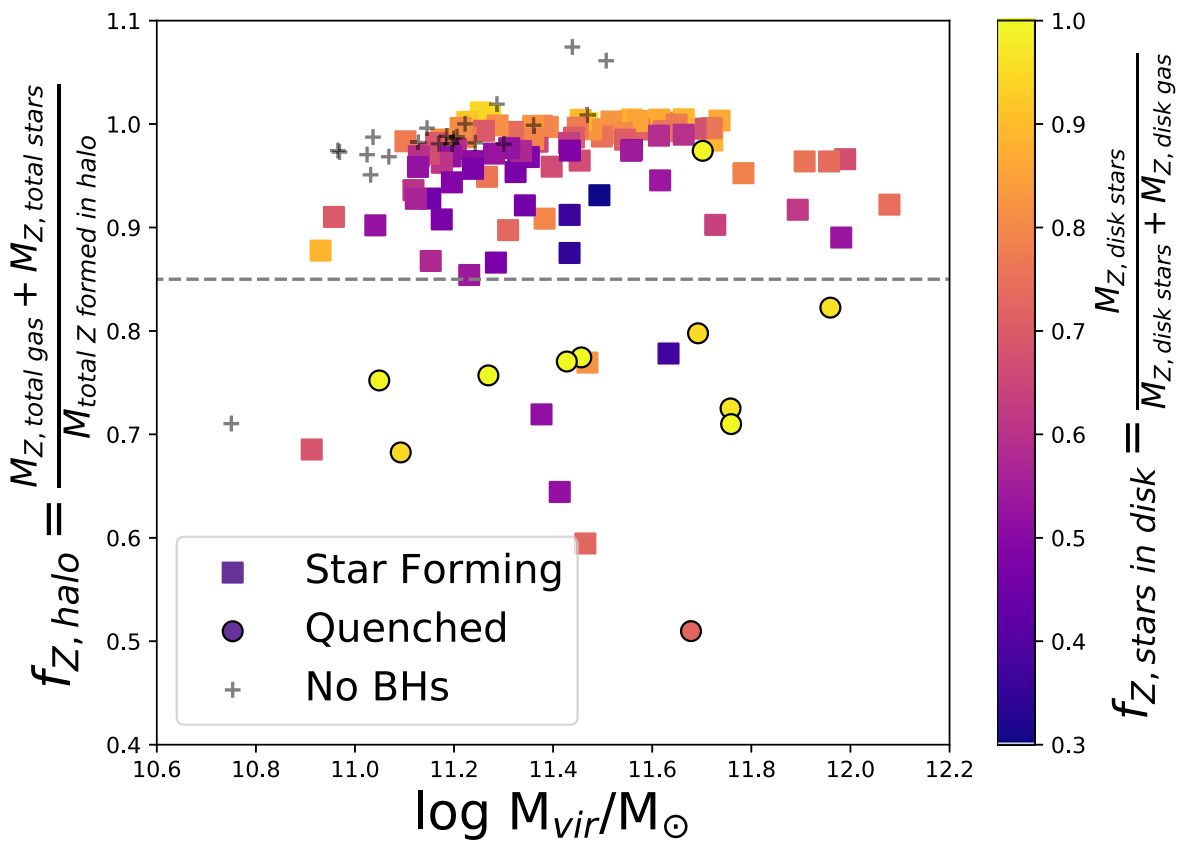


Figure 3. The fraction of all metals retained in the halo, $f_{Z,halo}$, as a function of the galaxy halo mass colored by the fraction of disk metals locked in stars. Most of the SF galaxies (squares) retain at least 85% of their total formed metals with a few (6/119 SF galaxies) losing more. Meanwhile, Q galaxies (circles) lose anywhere from 0% to 50% of their metals. We include the galaxies with no BHs (gray crosses) within R25 that reside within our mass range and note they are on the lower-mass end. They maintain nearly all metals originally formed by the stars in their host galaxies and, in two cases, have gained additional metals.

responsible for ejecting metals out from the disk, but may also play a role in stellar regulation, by suppressing the overall star formation and therefore resulting in lower-metallicity stars at the host galaxy's center at z=0. This result is consistent with Sharma et al. (2022), who looked at the impact of SMBHs on galaxies in the dwarf mass regime, $M_*=10^8-10^{10}\,M_\odot$. They found that in the galaxies at the high-mass end of their sample $(M_*>10^{9.3}\,M_\odot)$, SMBHs are driving gas out from the central $0.1R_{\rm vir}$ into the CGM on fast timescales (~1 Gyr) around $z\sim0.5-1$.

However, Figure 3 shows distinct differences between the metal retention of Q galaxies and that of SF galaxies. All but one Q galaxy have lost some metals to the IGM, and nearly half of these have lost at least 15% of their total metals (circles under the dashed horizontal line). Additionally, every Q galaxy has over 70% of its metals locked in stars (yellow-to-orange circles). This characteristic likely comes from the fact that these Q galaxies have lost most if not all of their cold gas by $z \sim 0$. Thus, the primary contribution of metals comes from the stars that remain. Finally, two of the galaxies without BHs (gray crosses) in Figure 3 end up gaining a small fraction of metals over their lives.

The left panel of Figure 4 more clearly shows the distribution of metals within each galaxy component. It compares the metal retention in the CGM to the metal retention in the disk. Galaxies that fall along the gray one-to-one line have maintained all of their metals within the virial radius (a *y*-value of 1.0 in Figure 3). Since we know that most of our galaxies do not lose many metals to the IGM, it is unsurprising

that most galaxies fall nearly along this line. The points are colored by each galaxy's $\Delta M_{\rm BH}$, with red points indicating galaxies with the most overmassive BHs and blue points indicating the most undermassive BHs. As expected, the galaxies that retain the most metals in their disks (bottom right) have undermassive BHs, and from Figure 2 we know that the metals in their disks are locked primarily in stars. In contrast, the galaxies with overmassive BHs (red) have a larger fraction of their disk/central region metals stored in the gas phase (up to 70%), in addition to losing more of those metals to the CGM and some to the IGM as well. Thus, the populations of galaxies with over- and undermassive BHs are also distinguished by where the metals are stored inside their inner $0.1R_{\rm vir}$. In other words, galaxies hosting overmassive SMBHs have more of these metals in the gas phase, while galaxies with undermassive SMBHs have the largest fractions of the metals in this region

The right panel of Figure 4 shows the fraction of baryons in the CGM as a function of the baryonic fraction in the disk (points and colors as in the left panel). The gray line indicates where the baryonic fraction of the disk and the baryonic fraction of the CGM equals one. Unlike the metal retention plot to the left, we see some scatter above and below this line. This difference is due to using the cosmic baryon fraction to calculate the expected $M_{\rm total\ baryonic}$.

Comparing the left and right panels in this figure, we see that the metals in the galaxy do not generally trace the baryonic component. When examining the metal retention plot (Figure 4, left panel), we see that most galaxies fall along or below the

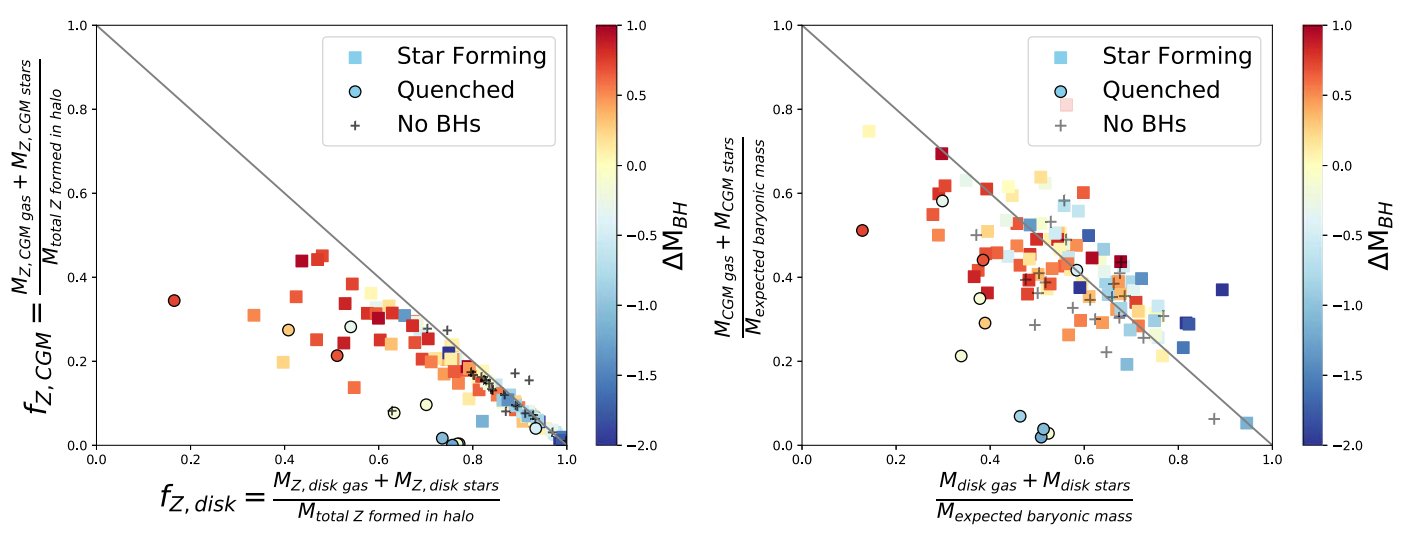


Figure 4. Left: the metal retention of gas and stars in the CGM as a function of the metal retention of gas and stars in the disk colored by the quantity $\Delta M_{\rm BH}$. The gray solid line indicates the one-to-one line where halos that fall along the line retain all of their the metals while halos below the line have lost metals to the IGM. This plot shows us that the SF galaxies with overmassive BHs (red squares) lose more metals into the CGM and in some cases out to the IGM. Meanwhile, the galaxies that retain the most metals in their disks host undermassive BHs (blue squares). Galaxies with no BHs appear to occupy a similar range as galaxies with undermassive BHs. All but one of the Q galaxies (circles) have lost over 20% of their metals from their central regions. Right: fraction of total baryonic mass in the CGM as a function of the fraction of total baryonic mass in the disk. The total baryonic fraction is relative to the cosmic baryon fraction. The points are colored by $\Delta M_{\rm BH}$. The gray line indicates where the sum of the baryonic fraction of the disk and the baryonic fraction of the CGM equals one. We note that nearly all the Q galaxies fall below this gray line, perhaps as a result of a loss of disk gas that results in their quenching. For SF galaxies, we find that galaxies with overmassive BHs (red squares) appear to have more baryons in the CGM compared to the galaxies with undermassive BHs (blue squares). Galaxies with no BHs (gray crosses) lie along the one-to-one line and have a scatter similar to the galaxies with undermassive BHs.

gray line and show a distinct trend with $\Delta M_{\rm BH}$. Meanwhile, the baryonic fractions are quite different. Though the measurements are centered on the gray line, they otherwise have significant scatter above and below and the trend with $\Delta M_{\rm BH}$ is not as pronounced. Nevertheless, galaxies with undermassive BHs (blue) tend to have more mass than expected and larger fractions of baryons in their disks (above the gray line) compared to galaxies with overmassive BHs, which have baryon fractions below their expected masses and tend to have a higher fraction of baryons in their CGM. Thus, the galaxies can accrete more than their expected share of baryons or have reduced baryons due to lower accretion, rather than expulsion from their halos (which would result in lower metal retention rates beyond what we find). The differences we see between these plots tell us that the motion of the metals is not strictly following the motion of the gas and stars in the galaxy.

Furthermore, we find that the galaxies with overmassive SMBHs are also those that are growing their SMBH through earlier accretion. Figure 5 (lower panel) shows the median values of our two subsamples for the cumulative sum of the accreted mass as a fraction of the total accreted mass for each central SMBH. The upper panels of Figure 5 show these values for each individual galaxy from which the median is calculated. We see that on average galaxies with overmassive BHs (red line) accrete material and grow their BHs at earlier times than their counterparts with undermassive BHs (blue line). This result is consistent with Sharma et al. (2020) and implies that there may be different avenues for the growth and formation of these SMBHs. Furthermore, Sharma et al. (2020) find that the different timescales of galaxy growth are related to their halo concentration.

3.1.2. AGN Feedback Flattens Mass and Metallicity Gradients

Within this lower-mass half of our galaxy sample, we have shown that galaxies with differences in their SMBH mass residuals ($\Delta M_{\rm BH}$) have different fractions of metals in the CGM. Within each galaxy, we measure the total energy output through SMBH feedback, as in Equation (1), and stellar feedback, as in the simulation accounting for feedback from SNe Ia and II (for more details, see Stinson et al. 2006). We compare the ratio of these two quantities in Figure 6. Though stellar feedback dominates in all galaxies, we find that the galaxies with overmassive SMBHs (red) experience more AGN feedback comparatively, even at the low-mass end. From Figure 6, we argue that the feedback from SMBHs is responsible for impacting the local redistribution of metals in these galaxies, not stellar feedback, likely due to the buildup of metals at the galaxies' centers (Figure 7). Furthermore, we argue that overmassive SMBHs are more effective at redistributing mass in galaxies with comparatively smaller potential wells, which can explain the differences in metal retention that we see in Figure 2. Finally, this result provides further evidence for the importance of AGN-driven outflows in low-mass galaxies, as shown by other simulation groups (Koudmani et al. 2019, 2021; Wellons et al. 2023).

This process additionally impacts each galaxy's mass and metallicity gradients. We split the sample into two bins, which include all the galaxies in the low-mass sample with overmassive BHs ($\Delta M_{\rm BH} > 0$) and those with undermassive SMBHs ($\Delta M_{\rm BH} < 0$). Figure 7 shows the median gas-phase (left) and stellar metallicity (right) profiles for all the galaxies with overmassive BHs (red) and those with undermassive BHs (blue). We also include the median metallicity gradients for the population of galaxies with no central SMBHs in gray. We see that, on average, galaxies with undermassive BHs or no BHs are more likely to have a concentration of metals built up within the gas and stars in their centers. Galaxies with no BHs are less massive, on average, resulting in lower central metallicity profiles, but overall they have a profile and slope closer to that of the galaxies with undermassive BHs. By

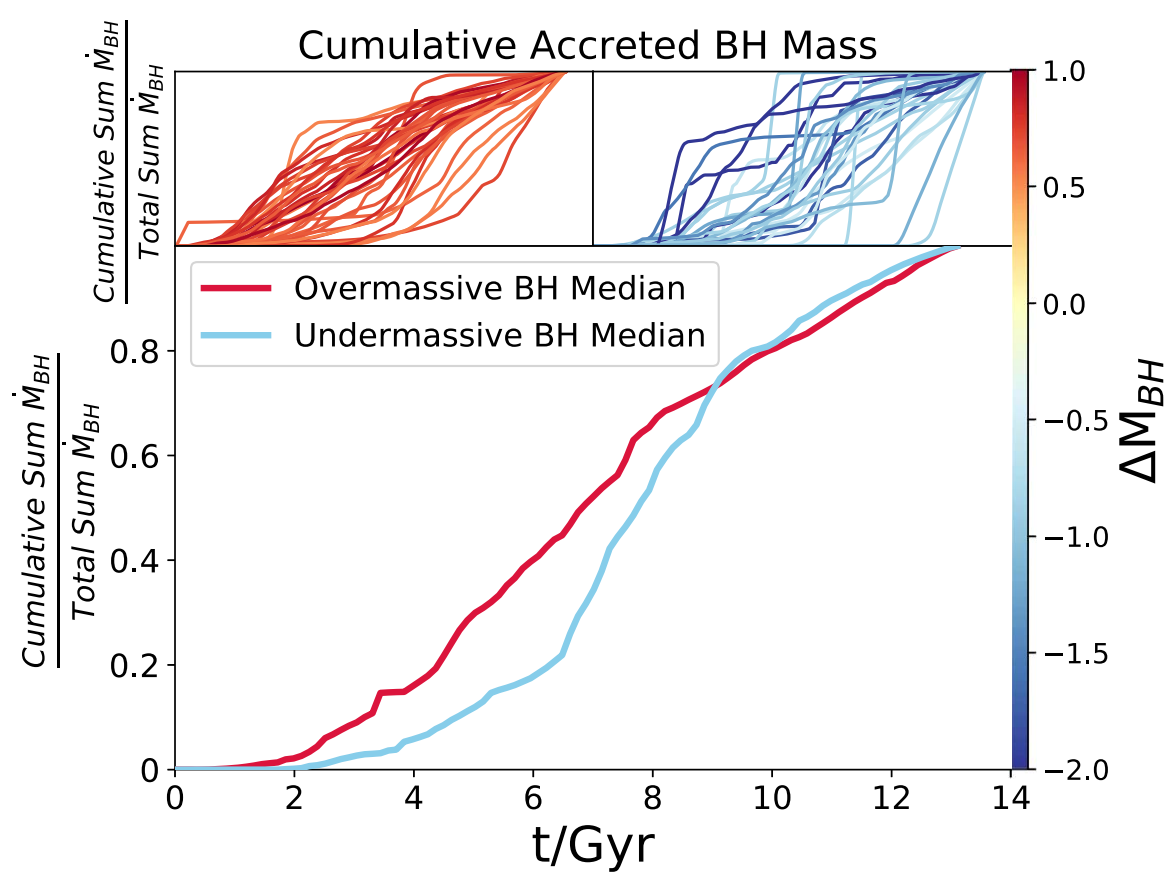


Figure 5. The cumulative sum of the accreted BH mass as a fraction of the total accreted BH mass as a function of time. Upper panels: the red and blue lines correspond to these values for each individual galaxy with an over- or undermassive BH, respectively. Lower panel: the red and blue lines correspond to the median values for the galaxies with overmassive BHs and undermassive BHs, respectively. Here, we have only included BHs with $|\Delta M_{\rm BH}| > 0.5$ to select for galaxies with the most significant mass deviation. We find that galaxies with overmassive BHs grow earlier than galaxies with undermassive BHs. Sharma et al. (2020) find that the timing of galaxy growth is related to halo concentration.

comparison, galaxies with overmassive BHs have fewer metals in their centers and have an overall flatter metallicity profile on average, likely driven by the evacuation of metals by the SMBH.

In Figure 8, we additionally compare the gas mass and stellar mass radial profiles for this split sample. We see a similar stellar mass profile shape for both the populations of galaxies with over- and undermassive BHs; however, the galaxies with undermassive BHs have a larger buildup of stellar mass in their centers, by about half a dex. In the gas-mass profile, we find that both the galaxies with undermassive BHs and without BHs have very similar profiles. In the stellar mass profiles, the median profile for the galaxies without BHs is lower than the galaxies with undermassive BHs, likely due to the lower average galaxy mass of the no-BH sample. However, we argue that the shape of the stellar mass profile for the galaxies without BHs is closer to that of the galaxies with undermassive BHs. Additionally, the profile for galaxies without BHs is lower, as they are likely to be less massive, given that the occupation fraction decreases with decreasing stellar mass.

These profiles help explain what we see in the galaxies with undermassive BHs. These galaxies have SMBHs that grow to smaller masses than expected for their stellar velocity dispersion/potential (Figure 1). These undermassive BHs are less effective at regulating star formation across the evolution of the galaxy, which results in two of the characteristics we see:

the buildup of stellar mass and both stellar and gas-phase metallicity buildup in the center of the galaxies.

Thus, due to less feedback from the SMBH, more metals end up locked in both the the gas and stars at the centers of the galaxies with undermassive SMBHs and more stars form over all. This point further confirms one of the results of Sharma et al. (2020), which finds that the hosts of undermassive BHs followed nearly identical evolutionary tracks to galaxies without BHs. This result is also consistent with Sanchez et al. (2019), who show that galaxies without BH physics end up with a significant buildup of metals in their cores, without BH feedback to eject the metals from the center and suppress star formation.

3.1.3. AGN Feedback Does Not Evacuate Gas from the CGM

We have shown that the local redistribution of mass by the SMBH in our galaxy sample impacts the metal retention in the disk and the metallicity profiles of our galaxies. To understand the impact of AGN feedback on the CGM of these galaxies, we compare our results to those of Davies et al. (2020), who find that galaxies with overmassive BHs have a lower fraction of baryons in their CGM, due to the evacuation of gas by BH feedback both for IllustrisTNG galaxies and those from the EAGLE simulation. Interestingly, we find our results are quite different. Figure 9 shows the fraction of baryons in CGM gas,

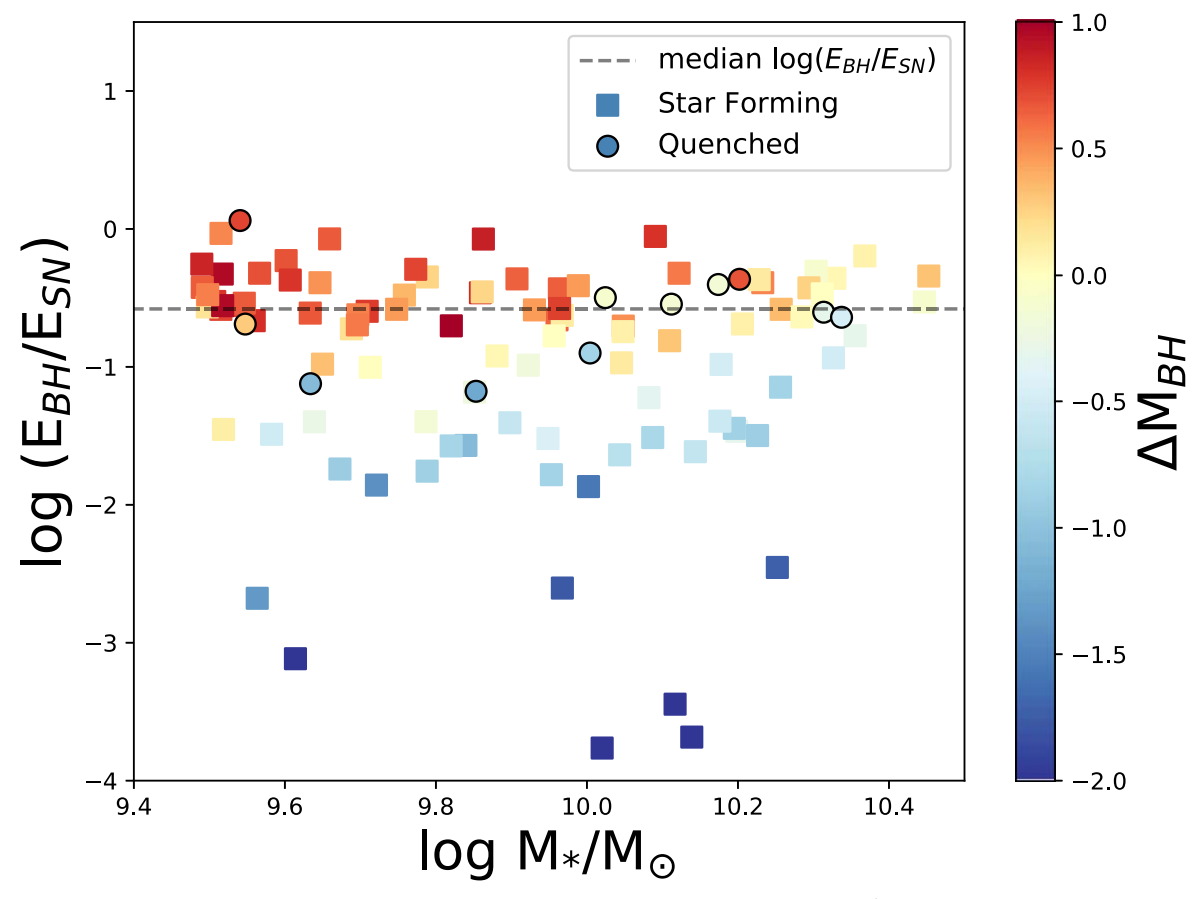


Figure 6. The ratio of SMBH and stellar feedback energy as a function of stellar mass. The points are colored by $\Delta M_{\rm BH}$. The dashed line indicates the median of the ratio of SMBH and stellar feedback energy, and galaxies that fall above this line have more AGN feedback than average. The galaxies with overmassive BHs (red) lie above this line, even at the low-mass end, indicating that the impact of SMBH feedback, not stellar feedback, is resulting in the differences in metal content that we see at the centers of these galaxies.

defined as in Davies et al. (2020):

$$f_{\rm CGM} = \frac{M_{\rm CGM}}{M_{\rm vir}},\tag{8}$$

where M_{CGM} is the gas mass within M_{vir} that is not starforming. Interestingly, we find no correlation with f_{CGM} and the over- or undermassive states of the SMBHs from our galaxies.

This distinct differences between our findings and those of Davies et al. (2020) are likely due to the differences in the implementation of subgrid BH physics. In the EAGLE simulation, AGN feedback (Booth & Schaye 2009) is implemented via stochastic, isotropic heating applied to gas particles ($\Delta T_{\rm AGN} = 10^{8.5}$ K), and the AGN feedback efficiency was chosen to reproduce the z=0 scaling relation between galaxies' stellar masses and their central SMBH masses. The energy injection rate is $f_{\rm AGN} \dot{m}_{\rm acc} c^2$, where $\dot{m}_{\rm acc}$ is the BH accretion rate and $f_{\rm AGN} = 0.015$ is a fixed value, where $f_{\rm AGN}$ determines the fraction of available energy coupled to the ISM. AGN feedback is the primary form of self-regulation in EAGLE once a hot CGM has formed, limiting the impact of stellar-driven winds out of the galaxy (Bower et al. 2017).

In IllustrisTNG, AGN feedback is implemented in two modes: high accretion rates drive a feedback mode that injects energy thermally, heating nearby gas cells to the BH using an efficiency of $f_{\rm AGN,thm} = 0.02$, which is similar in scheme to our implementation in R25. Meanwhile, feedback associated with low accretion rates injects energy kinetically, with a random

direction chosen for each injection event. The efficiency of the kinetic mode, $f_{\rm AGN,kin}$, scales with local gas density up to 0.2, and the kinetic AGN energy is injected with a velocity determined by the mass of gas associated with the injection region. The threshold between high and low accretion scales as a function of the BH mass and is written in terms of the Eddington ratio:

$$\chi = \min[0.1, \,\chi_0 (m_{\rm BH}/10^8 M_{\odot})^2],\tag{9}$$

where $\chi_0 = 0.002$. Regardless of mass, a BH can inject feedback via the thermal mode at sufficiently high accretion rates (Weinberger et al. 2017); however, once a BH reaches the pivot mass of $10^8 M_{\odot}$, this mode becomes rare, thereby setting this mass as the transition between thermal and kinetic feedback modes.

While the simulations discussed in Davies et al. (2020) find that the SMBHs effectively eject gas from the CGM out into the IGM, our results are quite different. We find that in our galaxies, the quantity f_{CGM} does not appear to be influenced by ΔM_{BH} . Thus, the majority of the SMBHs in our galaxies do not appear to evacuate gas and metals from the CGM out past the virial radius (as seen in Figure 3). The impact of the SMBH's feedback in relation to the depth of its host galaxy's gravitational potential (as sampled by stellar dispersion) does not appear to affect the baryon content of the CGM. Instead, we find that the mass and metal redistribution of the SMBH feedback is primarily limited to the local vicinity of the galaxy.

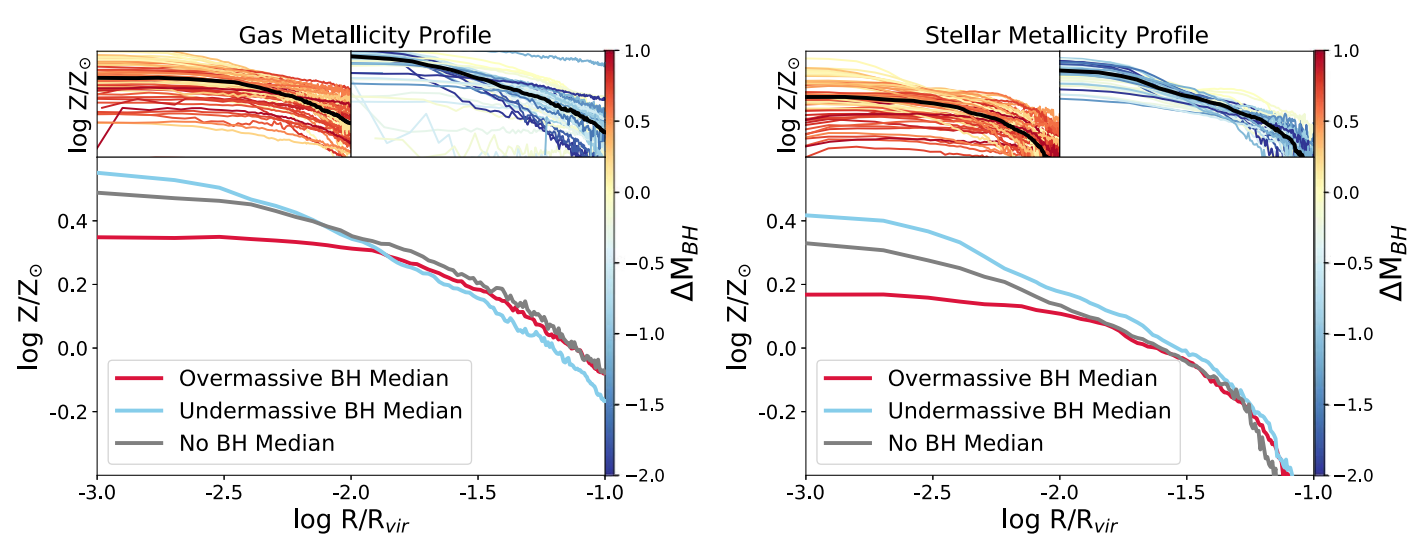


Figure 7. Median gas-phase metallicity (left) and stellar metallicity (right) profiles for the galaxies that host overmassive (red) and undermassive (blue) SMBHs in our sample, including the median values for each subsample (bottom plots). Profiles are calculated across 100 bins from r = 0.01 to $0.1R_{\rm vir}$. In both pairs of profiles, galaxies with overmassive BHs show a flatter distribution of metals, with no strong buildup of metals in the center. By comparison, galaxies with undermassive BHs tend to have a buildup of supersolar metal-rich gas at their centers and a steeper metallicity profile.

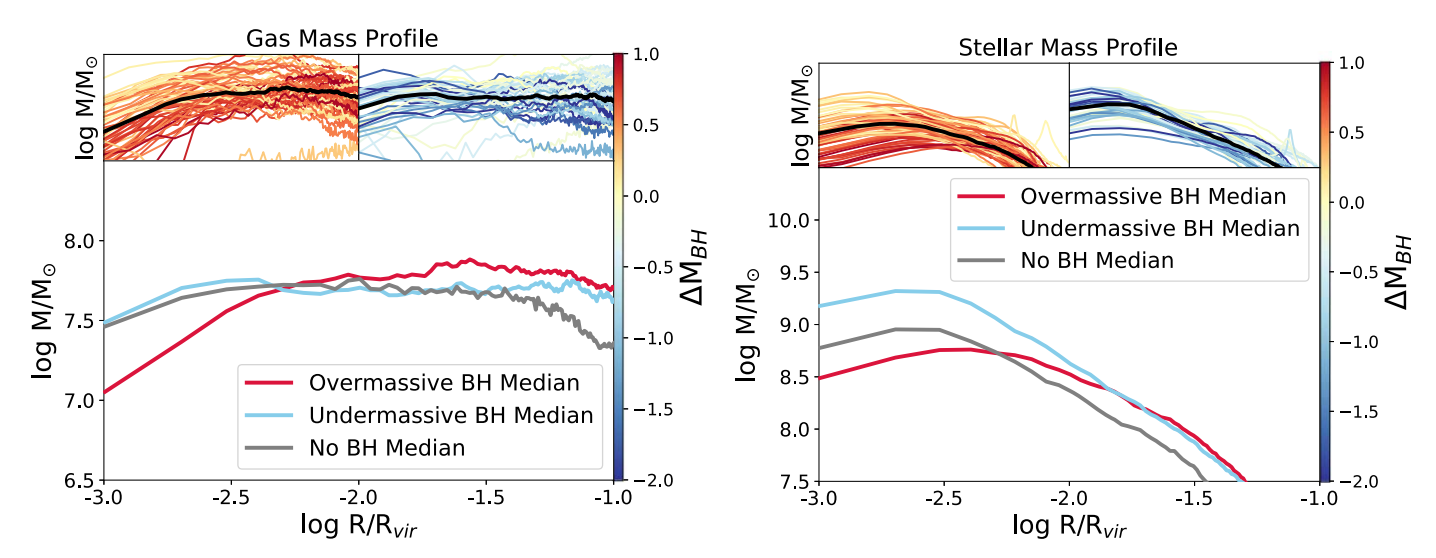


Figure 8. Gas-mass (left) and stellar mass (right) profiles for all the overmassive (red lines) and undermassive (blue lines) galaxies in our sample, including the median values for each subsample (bottom plot). Profiles are calculated across 100 bins from r = 0.01 to $0.1R_{\rm vir}$. Overall, the stellar mass profiles for galaxies with both overand undermassive SMBHs have a similar shape, but galaxies with undermassive BHs have about half a dex more mass in stars in their cores.

We note that the AGN feedback in R25 has been shown to be more moderate than in other cosmological simulations (Tremmel et al. 2019; Chadayammuri et al. 2021; Jung et al. 2022). It may be that in the absence of high-temperature metal cooling, our AGN can drive galaxy-scale outflows that can effectively regulate star formation but are not powerful enough to evacuate the CGM. We elaborate on this idea and its implications further in Section 4.1.

Nevertheless, the stark differences between the measurements of the baryonic content of the CGM between the two simulations and from other groups will be an exciting test for future observations that measure gas and metal abundances in the CGM and include dynamical measurements of SMBH masses. See Section 4 for additional discussion.

Interestingly, there appears to be a small population of galaxies between log $M_{\rm halo} = 10^{11-11.5}~M_{\odot}$ that have significantly lower values of $f_{\rm CGM}$ (Figure 9, bottom left). These galaxies also stand out in the right-hand panel of Figure 4 (blue

circles at bottom center), and we see that these galaxies have $\Delta M_{\rm BH} < 0$. These galaxies have nearly all of their metal and baryonic content within the inner $0.1R_{\rm vir}$ locked in stars, with little gas remaining in their centers. Sharma et al. (2022) explored the quenching in these and lower-mass dwarfs in R25. They find that galaxies with $M_* \sim 10^{10} M_{\odot}$, which are at the top of the dwarf mass regime, are more likely to experience quenching events that rapidly remove gas from the galaxy and partially evacuate the CGM within 1 Gyr. However, this characteristic effect appears to be confined to galaxies at or about $10^{10} M_{\odot}$ and is not seen in galaxies above or below this mass. See Sharma et al. (2022) for additional details.

3.2. Predictions for Observational Comparisons

To compare with both current and future observations, we create mock observations for metal retention measurements and predict C IV column densities for future surveys of quasar

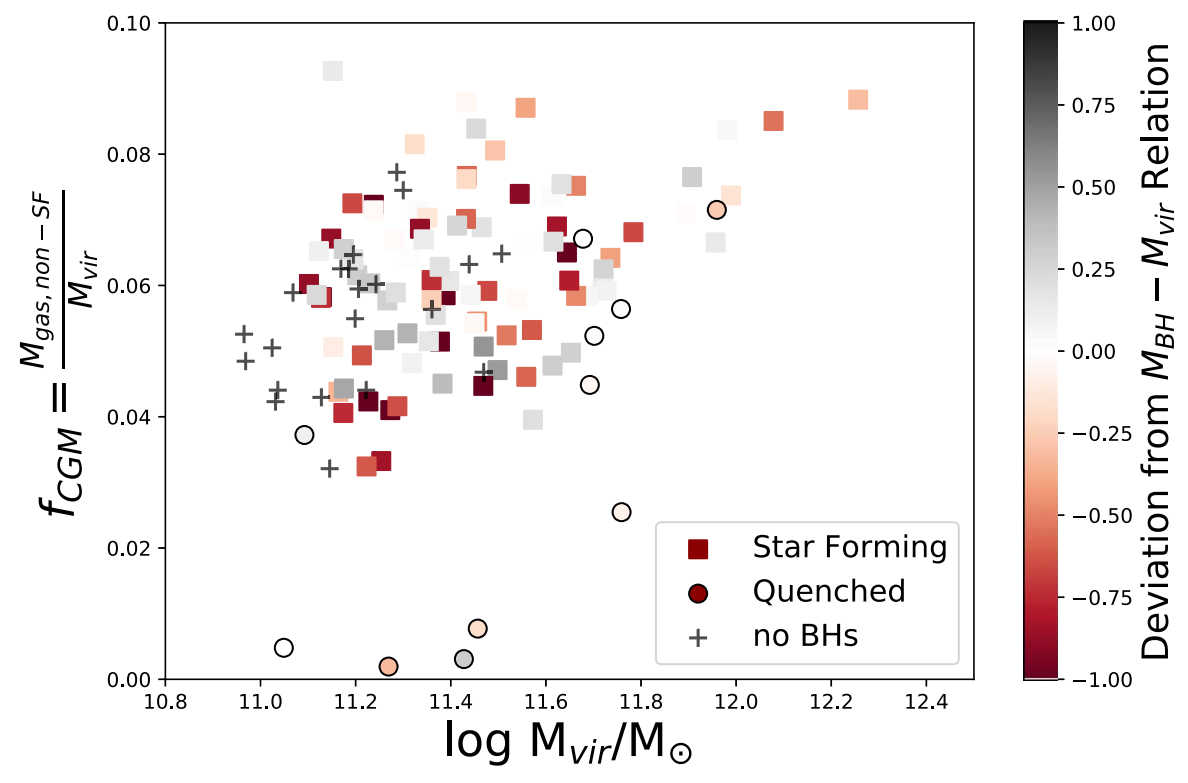


Figure 9. Measurements of the fraction of baryons in the CGM, as calculated in Davies et al. (2020), as a function of the virial mass for all 140 of our galaxies. To compare more accurately with Davies et al. (2020), the points in this plot are colored by the deviation of each SMBH's mass from the rolling mean of the $M_{\rm BH,acc}$ — $M_{\rm vir}$ relation (similar to Equation (6)). Unlike Figure 2 from Davies et al. (2020), we find no trend between the deviation from $M_{\rm BH,acc}$ — $M_{\rm vir}$ and $f_{\rm CGM}$ for our galaxies, indicating that at fixed halo mass, the deviation of the BH mass does little to impact the content of the CGM. We find a few Q galaxies with nearly fully evacuated CGMs (lower left circles), which is consistent with the rapid quenching (<1 Gyr) found by Sharma et al. (2022) on intermediate dwarf scales ($10^{9.3}~M_{\odot} < M_* < 10^{10}~M_{\odot}$).

spectroscopy that include dynamical mass measurements. For this section of the analysis, we include only the SF galaxies from our full galaxy sample, due to the small number statistics of our Q galaxies.

3.2.1. Mock Observations of Metal Retention

Within the same mass range of the R25 galaxies analyzed in this work, past observations have calculated average metal retention fractions within the disks of selected nearby galaxies of between 20% and 40% (Peeples et al. 2014; Telford et al. 2019). In comparison, the measurements for our simulated galaxies have an average of about 80%, as seen in Figure 2 and Table 1. To better compare to observations and determine whether our results could be confirmed observationally, we create mock observations of the stars and gas in the simulated galaxy disks and process them in the method of an observer. This process results in a set of new values for the metal retention fraction for each galaxy. We follow the method of Telford et al. (2019), as described below, to calculate the necessary components of the metal retention equation (Equation (4)), including the metal mass in the stars in the disk, the metal mass in the gas in the disk, and the metals produced by the stars in the disk. Then, we compare our mock observations to the results from our earlier method.

Figure 10 shows the stellar mass and gas-phase metallicity relation (the mass-metallicity relation, or MZR) for galaxies selected from R25 to show the validity of this mock observation analysis. The gray crosses show galaxies from R25 across 5 orders of magnitude and the black circles and white squares

indicate the same sample of galaxies we analyze throughout this paper. We find that the galaxies in R25 do follow the observed MZR of the Galaxy and Mass Assembly (GAMA) Survey (Foster et al. 2012) across the mass range of our galaxies, though our measurements are high compared to the Sloan Digital Sky Survey (SDSS; Kewley & Ellison 2008), depending on which calibration model is used to derive their metallicities (Pettini & Pagel 2004; Tremonti et al. 2004).

To move forward with our mock observations, we needed to construct "mock observed disks" from the simulated set of galaxies, including a stellar disk and gas disk. First, to select an "observed" stellar disk, we calculated the surface brightness of each galaxy, used the detection limit of SDSS (26 mag arcsec⁻²) to define the radius, and included all star particles within 1 kpc above and below the stellar plane. We use this definition of the stellar disk to calculate the star formation history (SFH) and the average stellar metal mass fraction in bins of 150 Myr for each galaxy. These are the mock observables, since an observer could measure these quantities by modeling the observed light from the stellar populations. From these quantities, we calculate the metal mass locked into the stars formed in each time bin as the product of the total mass of long-lived stars formed per bin (assuming a returned fraction of R = 0.425; Vincenzo et al. 2016) and the average metal mass fraction of the stars in that bin. The sum over all time bins then gives the total metal mass locked into disk stars, as an observer would measure.

We then use the same SFH and stellar metal mass fractions to calculate the metal production history for each galaxy, adopting the metal production model of Telford et al. (2019).

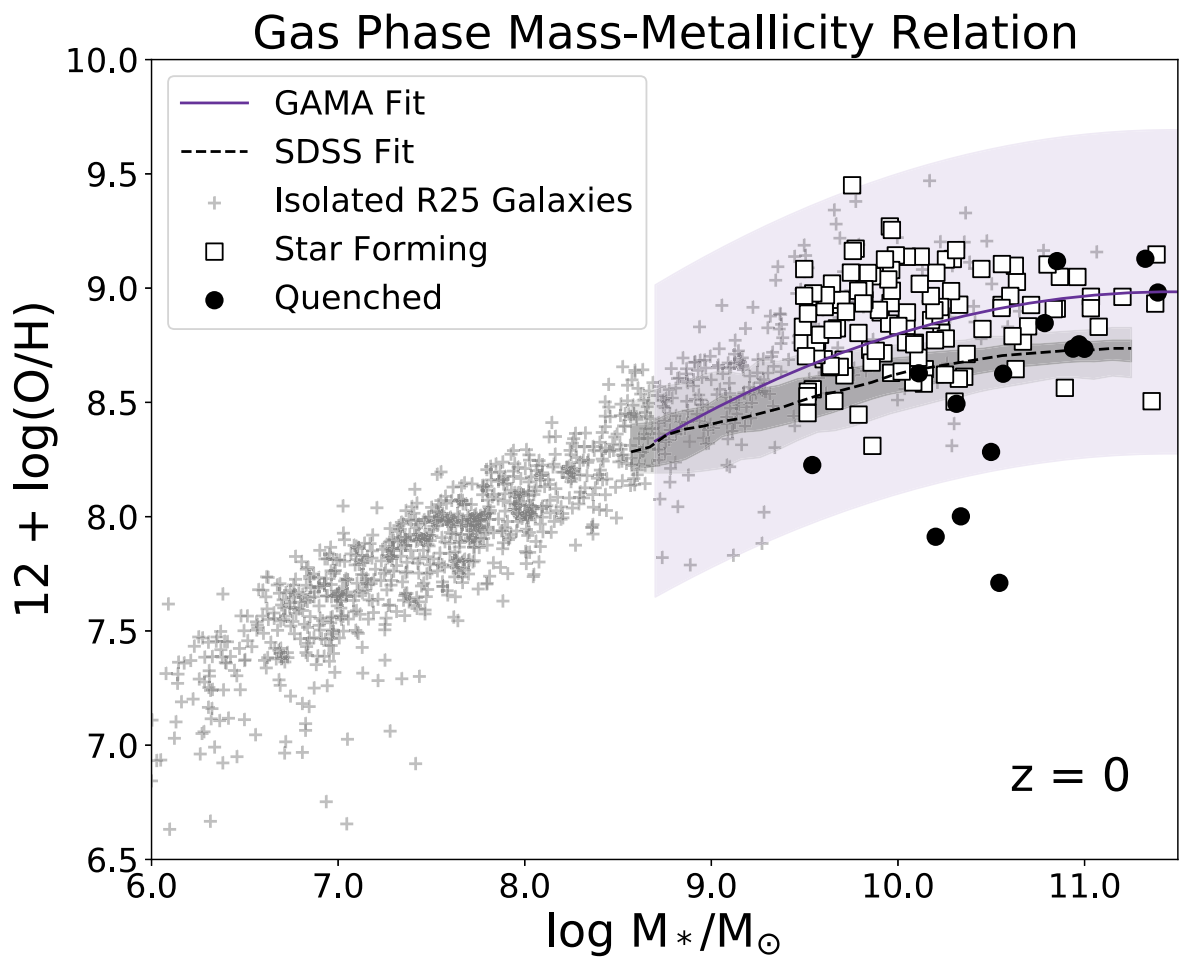


Figure 10. The relation between the stellar mass and gas-phase metallicity for our sample (black circles and white squares) and a wider selection of R25 galaxies (gray crosses) at z = 0. The black dashed line indicates the SDSS fit (Pettini & Pagel 2004; Tremonti et al. 2004) and the purple solid line indicates the same relation from the GAMA survey (Foster et al. 2012), with their errors in shaded purple. Our sample of galaxies $(3 \times 10^9 \, M_\odot < M_* < 3 \times 10^{11} \, M_\odot)$ fit well within the errors of the expected gas-phase metallicity of the galaxies from the GAMA survey, but overpredict the amounts expected from SDSS.

We do not attempt to match the metal production scheme in R25; rather, we opt to apply typical assumptions that an observer would make when calculating the metal mass produced by stars in an observed galaxy. We refer the reader to Section 3.1 of Telford et al. (2019) for details, but briefly summarize the key assumptions here. We account for metal production by Type II and Type Ia SNe, but exclude the contribution of AGB stars. For Type II SNe, we adopt metal yields from Nomoto et al. (2013) and account for the modest impact of stellar metallicity on predicted yields, and we assume that only stars $\leq 40M_{\odot}$ return metals to the ISM. For Type Ia SNe, we adopt the metal yields of Tsujimoto et al. (1995) and the delay time distribution of Maoz & Mannucci (2012), and we assume that the first Type Ia SN explodes 100 Myr after the onset of star formation. Using these ingredients, we construct a model of the metal production rate as a function of time following an instantaneous burst of star formation normalized to $1M_{\odot}$ formed, then convolve this model with the observed SFH to calculate the metal production history. Finally, we integrate the metal production history over time to obtain the total metal mass produced by the stars in the observed disk for each galaxy.

Then, to select an "observed" gas disk, we used a surface density cut in H I of 10^{17} cm⁻² and similarly included all the gas particles within 1 kpc above and below the disk plane. We

note a caveat of our work: molecular hydrogen is not separately calculated, due to the resolution of the simulation; therefore, the simulated H I includes all cold/cool ISM material (see the additional details in Christensen et al. 2012). From this gas-disk selection, we calculate the total sum of the H I mass within the disk and the average metallicity of cold, dense disk gas $(T < 10^4 \, \text{K}, \, \rho > 0.2 \, m_p \, \text{cm}^{-3})$. The simulation does not resolve individual H II regions, but in real galaxies, the same gas in which star formation is ongoing is ionized by young, hot stars to produce the nebular emission from H II regions that observers use to measure the gas-phase metallicity. The total metal mass in the gas phase is then simply calculated as the product of the total "observed" gas mass and the average metal mass fraction in the cold disk gas for each galaxy.

The final outputs are measurements for mock observations of the following quantities:

- 1. the metal mass locked in stars, $M_{Z,\text{disk stars}}$;
- 2. the metal mass in the gas phase, $M_{Z,\text{disk gas}}$;
- 3. the amount of metals produced from the stars, $M_{\text{total } Z \text{ formed in disk}}$;

and from those values we calculate a metal retention fraction, $f_{Z,disk}$, as in Equation (4).

The first three measurements are compared in Figure 11 for the measurements directly from the simulation and the mock

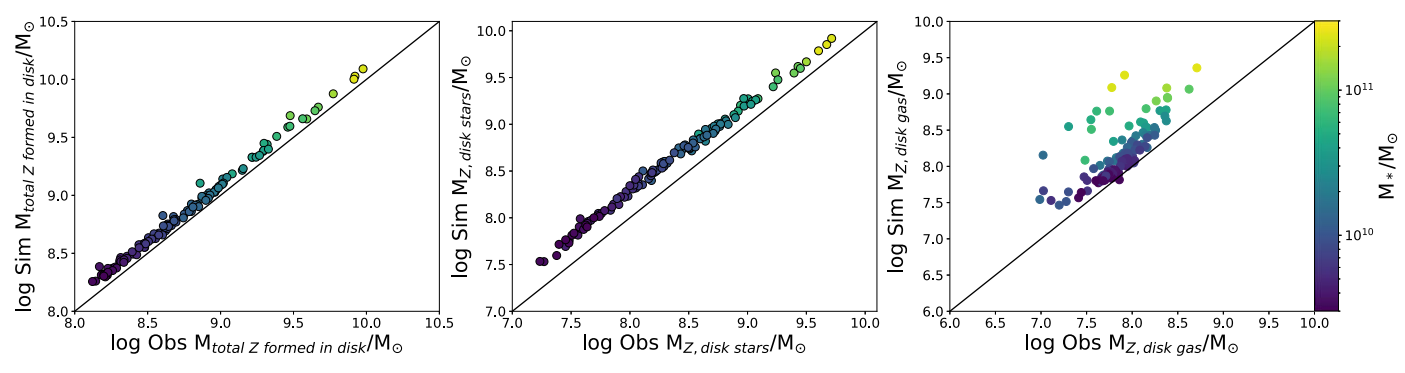


Figure 11. Comparisons between the simulation measurements and the mock observations for the $M_{\text{total }Z \text{ formed in disk}}$ (left), $M_{Z,\text{disk stars}}$ (middle), and $M_{Z,\text{disk gas}}$ (right). The mass of the total metals formed and the metal mass in stars track each other well, besides a small systematic offset due to the different definitions of the stellar disk in either case. The metal mass in the disk gas, however, shows a more significant offset, as well as more scatter.

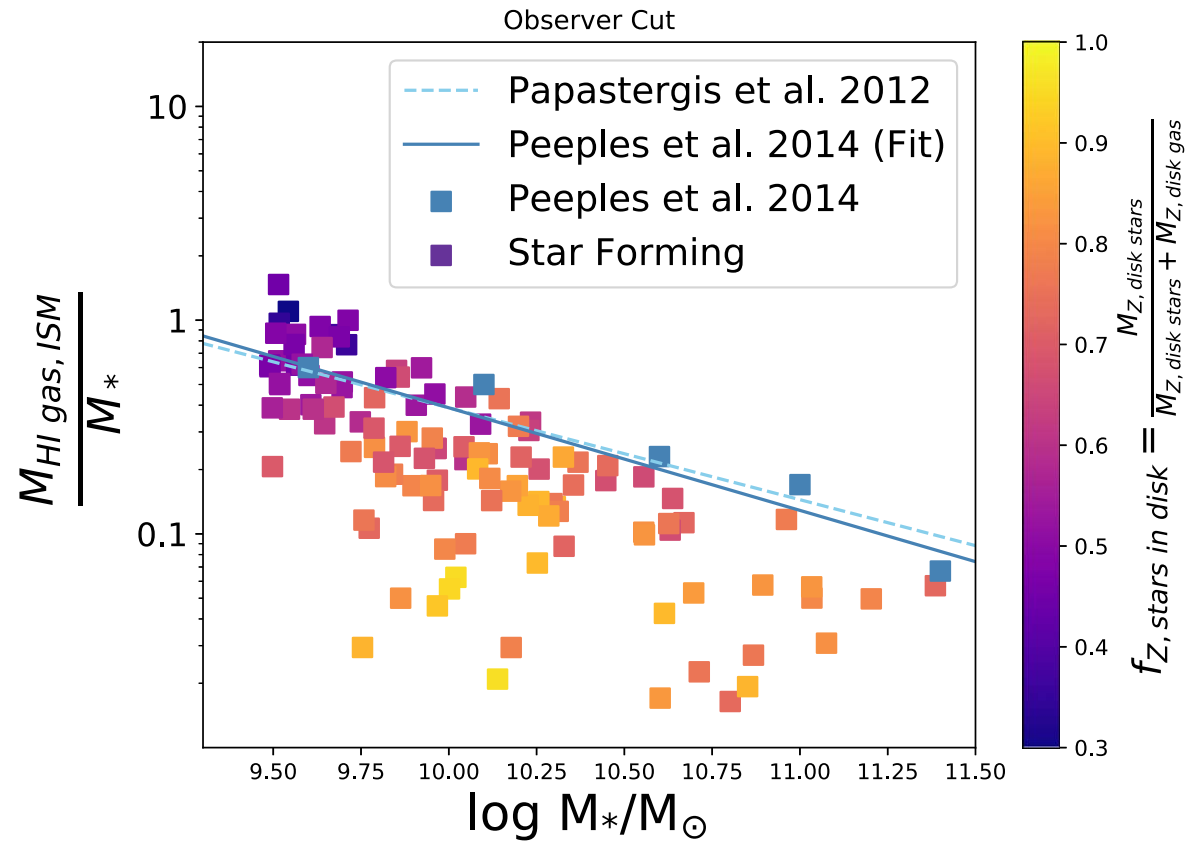


Figure 12. The fraction of mass in H I gas to stellar mass within our SF simulated galaxies as a function of their stellar mass. Observational constraints are included in the dashed blue (Papastergis et al. 2012) and solid blue lines and blue squares (Peeples et al. 2014). We find that our galaxies well match the observations at the lower-mass end of our SF sample; however, the H I gas mass fraction decreases to below expected values above $M_* > 10.25 M_{\odot}$ and shows more scatter at this high-mass end.

observation. In the leftmost plot, we compare the total metals formed in the disk, $M_{\text{total }Z \text{ formed in } \text{disk}}$, for the measurement from the simulation (y-axis) and the mock observation (x-axis) and see that these values are closely aligned. There are systematically more metals formed when calculated directly from the simulation, but this difference arises from the slightly different definitions of the stellar disk: $0.1R_{\text{vir}}$ versus the surface brightness cut at 26 mag arcsec⁻². Similarly, we see a difference in the middle plot of Figure 11 that shows the metal mass in the disk stars, $M_{Z,\text{disk stars}}$, with the measurement from the simulation showing more metals in the disk stars than the mock observations. Again, this difference comes from the variation in the definition of the stellar disk.

The rightmost plot of Figure 11 shows the quantity with the largest scatter. The simulated and mock observations of $M_{Z,\text{disk gas}}$ show significant scatter as well as a systematic offset. We determine that this offset is likely a result of using only the mass of H I gas rather than the total gas mass in the observer calculation. However, Figure 12 shows that the amounts of H I in the ISM of our galaxies are near the observed values at the low-mass end, though are lower at higher stellar masses. These low values of H I can be explained by referring back to the rightmost panel of Figure 11, which shows that galaxies with higher stellar mass lie farther from the one-to-one line in gray. This trend is a result of higher fractions of H II gas residing in the hotter halos of more massive galaxies and

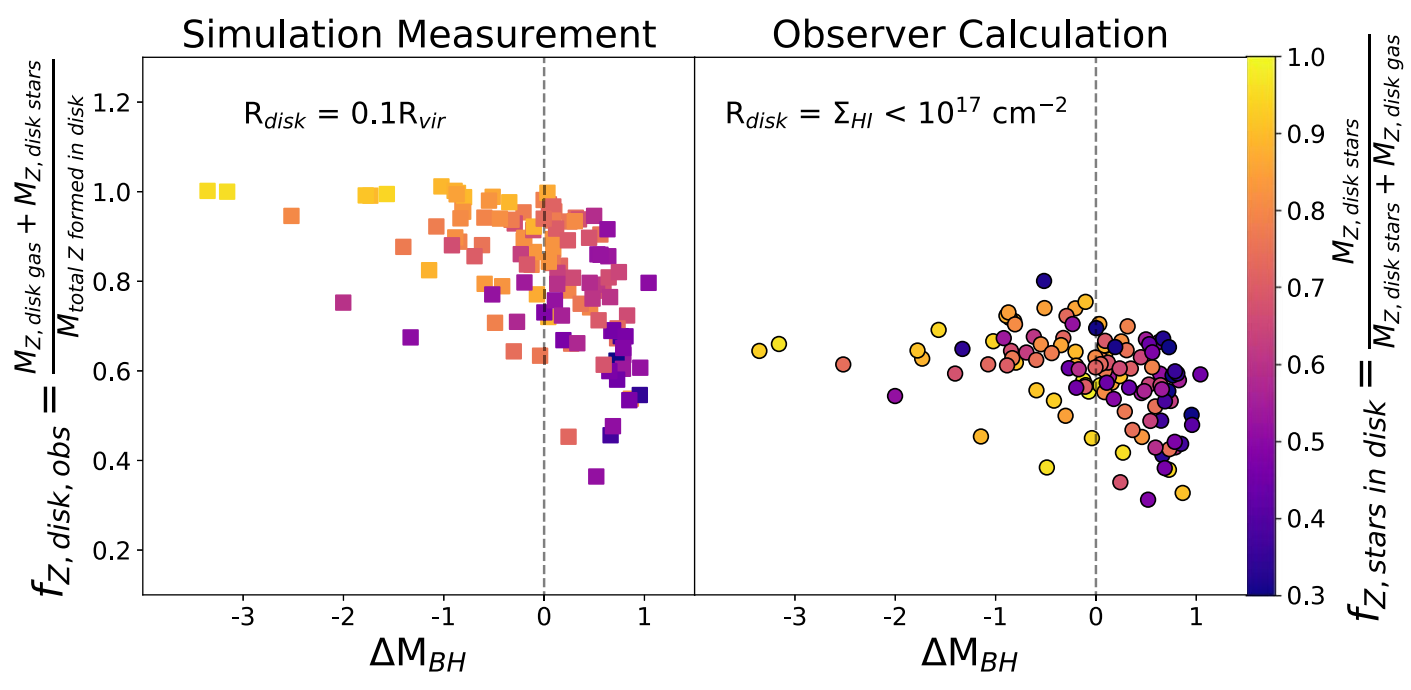


Figure 13. The metal retention fraction from the simulation (left, as in Figure 2) and the mock observations (right). Despite a difference in the median metal retention fraction, our results hold for the mock observations: galaxies with overmassive BHs have lower metal retention fractions than galaxies with undermassive BHs. It is possible that this result could be tested by comparisons to metal retention observations that have associated BH mass measurements.

thus depleting the amount of H I at these higher masses. It is likely that the inclusion of a full treatment of metal cooling could impact these results by increasing the total amount of cold gas traced by H I in our galaxy disks (Christensen et al. 2014).

Finally, we explore the impacts of these differences by comparing the metal retention fraction, $f_{Z,\mathrm{disk}}$, directly from the simulation and for the mock observations in Figure 13. In this figure (the left-hand panel of which reproduces Figure 2), we compare the metal retention fractions as functions of log ΔM_{BH} , with each point colored by the metal fraction of the disk/central region in stars for the simulated and mock observed quantities.

Both panels of Figure 13 have a qualitatively similar shape and show a flattened distribution below $\Delta M_{\rm BH} \lesssim 0$, though with significant scatter. However, the relation peaks at ~ 0.7 for the mock observations in the right panel instead of at 1 as in the left panel. In both cases, most of the galaxies that maintain more of their metals in stars (yellow points) have the highest metal retention fractions and host the most undermassive SMBHs. Galaxies that maintain the most metals in the gas phase of their disks are primarily galaxies with overmassive BHs (the purple points on the right-hand side of each panel). However, while the overall trend of undermassive BHs retaining more of their metals in their disk holds for the mock observations, we note that the trend with the metals locked in stars is present but not as clear.

Nevertheless, the relationship between $\Delta M_{\rm BH}$ remains broadly consistent (i.e., overmassive BHs result in lower metal retention in the disk). Thus, even with the biases inherent to the observational methods, there is potentially an observable separation between galaxies with high $f_{\rm Z,disk}$ values that host undermassive BHs compared to those with overmassive BHs with lower $f_{\rm Z,disk}$ values. However, the trend between galaxies

with metal-rich disk gas and different $\Delta M_{\rm BH}$ values is no longer as clear within the mock observations.

3.2.2. Column Densities of C IV

In addition to predicting how observable this effect may be through mock observations of metal retention, we also make predictions for how likely it might be to observe this phenomenon through quasar spectroscopy.

To do so, we calculate the column densities of C IV within the low-mass SF galaxy sample. We choose to measure C IV because it acts as a viable proxy for f_{CGM} , as it traces metals within gas with $T=10^4-10^5$ K and $\rho=10^{-5}-10^{-3}$ cm⁻³ at z=0 (Schaye et al. 2003; Oppenheimer & Davé 2006; Davé & Oppenheimer 2007; Ford et al. 2013; Rahmati et al. 2016; Oppenheimer et al. 2020b). Then we subdivide the SF galaxies into the two sets: galaxies with undermassive BHs and galaxies with overmassive BHs. Finally, we select matching pairs from each set with the closest available stellar masses to eliminate bias due to differences in stellar mass. This selection resulted in a subsample of 62 galaxies, 31 each with over- or undermassive SMBHs, from which we could specifically isolate differences due to the SMBH mass excess.

For each of these 64 galaxies, we then calculated the C IV column densities, $N_{\rm C\,IV}$, of their inner $0.1R_{\rm vir}$. Column densities of C IV are calculated using the publicly available analysis software PYNBODY (Pontzen et al. 2013). Oxygen and iron enrichment from SNe and winds are traced throughout the integration of the simulation and carbon abundances are calculated from Asplund et al. (2009). Ionization states are calculated during post-processing and assume optically thin conditions, collisional ionization equilibrium, and a UV radiation field at z=0 (Haardt & Madau 2012). Finally, we create models with variable temperature, density, and redshift using the CLOUDY software package (Ferland et al. 2013) to determine the fraction of C IV in each gas particle.

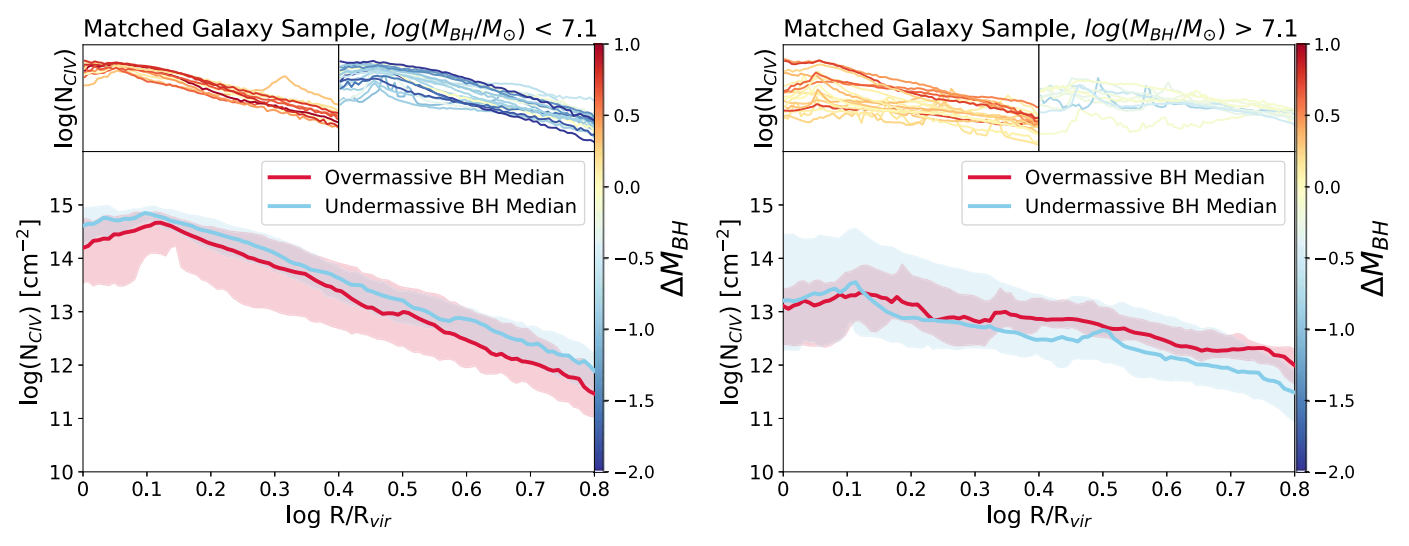


Figure 14. Column densities of C IV as a function of radius for the subsample of stellar-mass-matched galaxies with overmassive (red) and undermassive (blue) SMBHs. The shaded regions indicate the 16th to 84th percentile values. Left: galaxies from our matched sample with BH masses below $10^{7.1} M_{\odot}$. The upper panels show $N_{\text{C IV}}$ for each subset of galaxies, split between over- and undermassive SMBHs, and the lower panel shows the median for each subset. Right: the same set of figures as in the left panel, but for galaxies with SMBH masses above $10^{7.1} M_{\odot}$. Our measurements predict that upcoming UV absorption missions including host galaxy SMBH information, such as the COS-Holes survey, may observe a small difference in the amount of C IV in their CGM. In galaxies with higher BH masses, galaxies with overmassive BHs may contain slightly more C IV in the outer CGM (up to a few 0.1 dex), while a smaller difference in the C IV content may be seen in galaxies with lower-mass BHs. However, these differences are small and our results indicate that C IV is likely not be a strong indicator of SMBH feedback. This finding is consistent with S. L. Garza et al. (2024, in preparation), which finds little evidence that the host galaxy C IV in the CGM trends with the characteristics of central SMBHs.

From our 62 stellar-mass-matched galaxies, we split the sample into galaxies with SMBH masses above and below the median mass of $log(M_{BH,acc}) = 7.1$, then we plot the column densities of C IV as a function of radius and compare the median values in Figure 14. In galaxies with lower-mass BHs (left panel), there appear to be slightly higher column densities of CIV in galaxies hosting undermassive BHs, with a consistent difference of about 0.1-0.2 dex throughout the content of the CGM. In galaxies with higher-mass BHs (right panel), we find that there is more abundant C IV in the CGM of galaxies with overmassive SMBHs (red lines) than those with undermassive SMBHs (blue lines) in the outer CGM. Each shaded region indicates the 16th to 84th percentile value for each subsample. In these galaxies with higher-mass SMBHs, the difference between the median values of N_{CIV} appears strongest between 0.3 and 0.8 $R_{\rm vir}$.

However, we note that the overall differences between $N_{\rm C\ IV}$ for either set are not significant and the errors on each sample mostly span the median values for both overmassive and undermassive SMBHs. Therefore, our results indicate that C IV is likely not a strong observational indicator for SMBH feedback. Furthermore, when we compare the entire sample of 62 matched galaxies directly, the differences between the column densities of C IV disappear.

Future HST/COS surveys will be able to determine whether these predictions are borne out by observations. COS-Holes (Werk et al. 2021), one such survey, connects the UV absorption measurements made with COS to dynamically resolved SMBH measurements for galaxies in the line of sight of the background quasar. Our result is consistent with the findings of S. L. Garza et al. (2024, in preparation), which publishes the first results from COS-Holes and finds no evidence of a strong connection between $N_{\rm C\,IV}$ and SMBH properties in local galaxies.

We discuss the implications of this result and compare our predictions to those from other simulations in Section 4.3.

4. Discussion and Conclusions

4.1. Metal Cooling May Erase Evidence of AGN Outflows

The lack of metal cooling in R25 is a major caveat of our results. The lack of metal-line cooling will result in an underestimate of the cooling rates of hot $(10^{5-6} \, \text{K})$ gas by a factor of a few (Shen et al. 2010). If metal cooling were included, it is possible that metal-enriched gas put into the CGM from AGN outflows may cool more rapidly and make its way back into the central galaxy. The lack of metal cooling in Romulus may artificially enhance the signature we see (less metals retained in the galaxy and more put into the CGM), while in reality this signature may be more transient.

However, we argue that our key result remains valid. The relationship between an SMBH's mass and its host's galactic potential (from σ by proxy) does determine how effective SMBH feedback is at driving outflows of metal-enriched gas from its host galaxy. For example, the galaxies with overmassive BHs will have their metals expelled from the galaxy and into the CGM; however, when metal cooling is included, the high fractions of metal-enriched CGM gas (as seen in Figure 4) may not be observed at $z \sim 0$, due to faster cooling times that allow that gas to cool back onto the galaxy more rapidly.

While the length of time that metal-enriched gas remains in the CGM may be overestimated by the cooling treatment in Romulus, our main result that scatter within the $M_{\rm BH}$ – σ relation is connected to the thermal and kinematic histories of metal-enriched gas still holds, with overly massive BHs more likely to drive larger outflows of metal-enriched gas farther into the CGM.

4.2. BHs Primarily Drive Metals into the CGM, Not the IGM

Sharma et al. (2020) looked at a sample of 205 isolated dwarf galaxies with central SMBHs from the R25 volume. They determined that galaxies with overmassive BHs formed earlier and exist in galaxies with lower stellar masses than expected for their halo. Despite exploring a higher-mass regime of galaxies, we see similar indications of lower stellar masses at the centers of our galaxies that host overmassive BHs, indicating that the BH may play a role in suppressing the integrated overall star formation of the galaxy. These results are also consistent with Davies et al. (2020), who found that in a sample of galaxies from EAGLE and IllustrisTNG, those with overmassive BHs formed within DM halos with tightly bound centers and were characterized by systematically lower SFRs.

However, Davies et al. (2020) found that the galaxies in their sample with overmassive BHs negatively correlated with the fraction of total gas in their CGM. In other words, galaxies that contain more massive BHs at fixed galaxy mass evacuate more of their CGM. In contrast, the total baryon fractions in the CGM of our galaxies do not correlate with the deviation of mass of our SMBHs. In fact, Figure 9 shows no trend with $\Delta M_{\rm BH}$ indicating that the overmassive BHs in our simulated galaxies are not evacuating the CGM, as is the case for EAGLE and IllustrisTNG. Instead, our results imply that the overmassive BHs in our galaxies may be effective at redistributing both gas and especially metals within the disk/central region ($\sim 0.1R_{\rm vir}$); however, these BH-driven outflows are not powerful enough to evacuate material out of the CGM and into the IGM, except in a few specific cases for galaxies with $M_* = 10^{10} M_{\odot}$ (Figure 9 of Sharma et al. 2022). The difference between our results and Davies et al. (2020) is likely a result of the different implementations of BH feedback we discussed in Section 3.

Interestingly, compared to studies from other simulation groups, our result remains an outlier. Work from Choi et al. (2020), which analyzes zoom-in galaxies run with the SPHGal code (Choi et al. 2017; a modified version of GADGET-3), also finds both gas and metals are evacuated out of galaxy halos via AGN feedback. Similarly, galaxies from the SIMBA simulation suite explored by Appleby et al. (2021) show significant CGM evacuation beyond $R_{\rm vir}$ via AGN feedback in galaxies above L_* masses.

From Figure 6, we confirm the SMBH's role in driving metals out of the center of the galaxy. This result is also consistent with the work of Sanchez et al. (2019), which explored the metal content of the CGM in a set of four galaxies run with the same code and nearly the same resolution $(M_{\rm gas}=2.1\times10^5~M_\odot,~M_{\rm DM}=1.4\times10^5~M_\odot)$ as R25. They compare four galaxy simulations with and without BH physics and find that the galaxies without BH physics end up with a concentration of metals in their centers, as we see here in the galaxies with undermassive BHs. Their Figure 10, which compares the metallicity profiles for ISM gas for the galaxies and shows a buildup of metals in the centers of the galaxies without BHs, is quite similar to our Figure 7. In our case, the galaxies with undermassive BHs show the same buildup of metals at the center as the galaxies with no BHs, which is consistent with Sharma et al. (2020). The consistencies between these simulations further confirm that the SMBH, which was responsible for ejecting metals from the galaxies in Sanchez et al. (2019), is also key in ejecting metals from the galaxies with overmassive BHs in our sample.

4.3. Predictions for Future CGM Surveys

From Figure 14, we predict that future surveys like COSHoles (Werk et al. 2021; S. L. Garza et al. 2024, in preparation) are unlikely to see a strong distinction between the amount of C IV and other ions in the CGM of galaxies that host over- and undermassive central SMBHs. However, additional observable tests for these predictions could come in the form of future HST/COS observations, like those of COS-Holes that pair UV absorption measurements to dynamical BH mass measurements for different ions in the CGM. With such observations, we may be able to determine whether or not SMBHs are evacuating gas in the CGM of their hosts. Furthermore, these kinds of metalline measurements, paired with dynamical BH mass estimates, would allow us to determine whether SMBHs that are over- or undermassive play different roles in setting the metal content of the CGM.

One compelling case is M31. Telford et al. (2019) measured the metals in the disk of the Andromeda galaxy and determined that it had lost up to 62% of the metals formed by its stellar population. Therefore, the metal retention of the disk, $f_{Z,\text{disk}}$, is 38%, which is within the range of the metal retention rates we find in our sample using the observer method (Figure 13, right). The galaxies with the lowest metal retention rates nearly all host overmassive BHs, which is the case for M31. M31 has a velocity dispersion in the bulge of 151–153 km s⁻¹ (Whitmore 1980; Zou et al. 2011) and a central SMBH mass of $1.4 \times 10^8 M_{\odot}$ (Bender et al. 2005), which is 1.5 times larger than expected, based on Equation (2) (Kormendy & Ho 2013).

While this is only one case, it demonstrates a clear example of a galaxy with metals that have been ejected from the disk in the presence of an SMBH that is overmassive compared to its stellar dispersion. Our study shows that there is plenty of exciting work to be done connecting the flow of metals in a galaxy to the properties and effects of its central SMBH.

Acknowledgments

We thank the anonymous referee whose detailed comments clarified and improved this paper. This work was supported by the FINESST19-23 grant 80NSSC19K1409 and NSF MPS-Ascend award ID 2212959. N.N.S. and J.K.W. acknowledge additional support for this work from NSF-AST 1812521, NSF-CAREER 2044303, and the Research Corporation for Science Advancement, grant ID No. 26842. Some of the predictions made in this study will inform the observational survey being carried out under HST-GO-16650, "Connecting Galaxy Black Hole Mass with the State of the Circumgalactic Medium." A collaborative visit was funded by the European Union's Horizon 2020 research and innovation program, under grant agreement No. 818085 GMGalaxies. T.R.Q. acknowledges support from Blue Waters and XSEDE, and the simulation in this study was run on NAS. Analysis was completed on NAS (under NASA award SMD-21-75544133). N.N.S. gratefully acknowledges helpful conversations with the following individuals: Andrew Pontzen, Jonathon Davies, Martin Rey, Hannah Bish, Ben Oppenheimer, Ferah Munshi, Jillian Bellovary, Anna Wright, and Julianne Dalcanton.

ORCID iDs

N. Nicole Sanchez https://orcid.org/0000-0001-7589-6188 Jessica K. Werk https://orcid.org/0000-0002-0355-0134

```
Charlotte Christensen \bigcirc https://orcid.org/0000-0001-6779-3429
```

```
O. Grace Telford https://orcid.org/0000-0003-4122-7749
Thomas R. Quinn https://orcid.org/0000-0001-5510-2803
Michael Tremmel https://orcid.org/0000-0002-4353-0306
Jennifer Mead https://orcid.org/0009-0006-4744-2350
Ray S. Sharma https://orcid.org/0000-0001-8350-4535
Alyson M. Brooks https://orcid.org/0000-0002-0372-3736
```

References

```
Alexander, D. M., Small, I., Bauer, F. E., et al. 2005, Natur, 434, 738
Alongi, M., Bertelli, G., Bressan, A., et al. 1993, A&AS, 97, 851
Anglés-Alcázar, D., Davé, R., Faucher-Giguére, C.-A., Özel, F., &
  Hopkins, P. F. 2017, MNRAS, 464, 2840
Appleby, S., Dav é, R., Sorini, D., Storey-Fisher, K., & Smith, B. 2021,
          S, 507, 2383
Asplund, M., Grevesse, N., Sauval, A. J., & Scott, P. 2009, ARA&A, 47, 481
Bender, R., Kormendy, J., Bower, G., et al. 2005, ApJ, 631, 280
Bertelli, G., Bressan, A., Chiosi, C., Fagotto, F., & Nasi, E. 1994, A&AS,
   106, 275
Booth, C. M., & Schaye, J. 2009, MNRAS, 398, 53
Borthakur, S., Heckman, T., Tumlinson, J., et al. 2015, ApJ, 813, 46
Bower, R. G., Schaye, J., Frenk, C. S., et al. 2017, MNRAS, 465, 32
Bressan, A., Fagotto, F., Bertelli, G., & Chiosi, C. 1993, A&AS, 100, 647
Chadayammuri, U., Bogdan, A., Oppenheimer, B., et al. 2022, ApJL, 936, L15
Chadayammuri, U., Tremmel, M., Nagai, D., Babul, A., & Quinn, T. 2021,
   MNRAS, 504, 3922
Choi, E., Brennan, R., Somerville, R. S., et al. 2020, ApJ, 904, 8
Choi, E., Ostriker, J. P., Naab, T., et al. 2017, ApJ, 844, 31
Christensen, C., Quinn, T., Governato, F., et al. 2012, MNRAS, 425, 3058
Christensen, C. R., Brooks, A. M., Fisher, D. B., et al. 2014, MNRAS,
   440, L51
Davé, R., & Oppenheimer, B. D. 2007, MNRAS, 374, 427
Davies, J. J., Crain, R. A., Oppenheimer, B. D., & Schaye, J. 2020, MNRAS,
Di Matteo, T., Springel, V., & Hernquist, L. E. 2005, Natur, 433, 604
Dubois, Y., Volonteri, M., Silk, J., et al. 2015, MNRAS, 452, 1502
Emsellem, E., Cappellari, M., Krajnović, D., et al. 2011, MNRAS, 414, 888
Ferland, G. J., Porter, R. L., van Hoof, P. A. M., et al. 2013, RMxAA, 49, 137
Ferrarese, L., & Merritt, D. 2000, ApJL, 539, L9
Ford, A. B., Oppenheimer, B. D., Davé, R., et al. 2013, MNRAS, 432, 89
Foster, C., Hopkins, A. M., Gunawardhana, M., et al. 2012, A&A, 547, A79
Gebhardt, K., Kormendy, J., Ho, L. C., et al. 2000, ApJL, 543, L5
Graham, A. W., & Scott, N. 2015, ApJ, 798, 54
Guedes, J., Callegari, S., Madau, P., & Mayer, L. 2011, ApJ, 742, 76
Haardt, F., & Madau, P. 2012, ApJ, 746, 125
Habouzit, M., Li, Y., Somerville, R. S., et al. 2021, MNRAS, 503, 1940
Haehnelt, M. G., Natarajan, P., & Rees, M. J. 1998, MNRAS, 300, 817
Hosokawa, T., Yorke, H. W., Inayoshi, K., Omukai, K., & Yoshida, N. 2013,
    ApJ, 778, 178
Howk, J. C., Wotta, C. B., Berg, M. A., et al. 2017, ApJ, 846, 141
Jung, S. L., Rennehan, D., Saeedzadeh, V., et al. 2022, MNRAS, 515, 22
Kewley, L. J., & Ellison, S. L. 2008, ApJ, 681, 1183
Kormendy, J., & Ho, L. C. 2013, ARA&A, 51, 511
Koudmani, S., Henden, N. A., & Sijacki, D. 2021, MNRAS, 503, 3568
Koudmani, S., Sijacki, D., Bourne, M. A., & Smith, M. C. 2019, MNRAS,
   484, 2047
Magorrian, J., Tremaine, S., Richstone, D., et al. 1998, AJ, 115, 2285
Maoz, D., & Mannucci, F. 2012, PASA, 29, 447
Menon, H., Wesolowski, L., Zheng, G., et al. 2015, ComAC, 2, 1
Micic, M., Holley-Bockelmann, K., Sigurdsson, S., & Abel, T. 2007, MNRAS,
Mitchell, P. D., Schaye, J., Bower, R. G., & Crain, R. A. 2020, MNRAS,
Moster, B. P., Naab, T., & White, S. D. 2013, MNRAS, 428, 3121
Moster, B. P., Somerville, R. S., Maulbetsch, C., et al. 2010, ApJ, 710, 903
Munshi, F., Governato, F., Brooks, A. M., et al. 2013, ApJ, 766, 56
Natarajan, P. 2011, BASI, 39, 145
Nelson, D., Kauffmann, G., Pillepich, A., et al. 2018, MNRAS, 477, 450
Nelson, D., Pillepich, A., Springel, V., et al. 2019, MNRAS, 490, 3234
Nomoto, B. D., & Davé, R. 2006, MNRAS, 373, 1265
Nomoto, K., Kobayashi, C., & Tominaga, N. 2013, ARA&A, 51, 457
Oppenheimer, B. D., Bogdán, Á., Crain, R. A., et al. 2020a, ApJL, 893, L24
```

```
Oppenheimer, B. D., Crain, R. A., Schaye, J., et al. 2016, MNRAS, 460, 2157
Oppenheimer, B. D., Davies, J. J., Crain, R. A., et al. 2020b, MNRAS,
  491, 2939
Oppenheimer, B. D., Segers, M., Schaye, J., Richings, A. J., & Crain, R. A.
  2018, MNRAS, 474, 4740
Papastergis, E., Cattaneo, A., Huang, S., Giovanelli, R., & Haynes, M. P. 2012,
    pJ, 759, 138
Papovich, C., Moustakas, L. A., Dickinson, M., et al. 2006, ApJ, 640, 92
Peeples, M. S., Werk, J. K., Tumlinson, J., et al. 2014, ApJ, 786, 54
Pettini, M., & Pagel, B. E. 2004, MNRAS, 348, 59
Planck Collaboration 2016, A&A, 594, 13
Pontzen, A., Roškar, R., Stinson, G. S., et al. 2013, pynbody: Astrophysics
   Simulation Analysis for Python, Astrophysics Source Code Library,
  ascl:1305.002
Pontzen, A., Tremmel, M., Roth, N., et al. 2017, MNRAS, 465, 547
Rahmati, A., Schaye, J., Crain, R. A., et al. 2016, MNRAS, 459, 310
Raiteri, C. M., Villata, M., & Navarro, J.F. 1996, A&A, 315, 105R
Reines, A. E., Greene, J. E., & Geha, M. 2013, ApJ, 775, 116
Reines, A. E., & Volonteri, M. 2015, ApJ, 813, 82
Ricarte, A., Tremmel, M., Natarajan, P., & Quinn, T. 2019, MNRAS, 489, 802
Ritchie, B. W., & Thomas, P. A. 2001, MNRAS, 323, 743
Rosas-Guevara, Y., Bower, R. G., Schaye, J., et al. 2016, MNRAS, 462, 190
Saglia, R. P., Opitsch, M., Erwin, P., et al. 2016, ApJ, 818, 47
Sales, L. V., Navarro, J. F., Schaye, J., et al. 2009, MNRAS, 399, L64
Sanchez, N. N., Bellovary, J. M., Holley-Bockelmann, K., et al. 2018, ApJ,
  860, 20
Sanchez, N. N., Tremmel, M., Werk, J. K., et al. 2021, ApJ, 911, 116
Sanchez, N. N., Werk, J. K., Tremmel, M., et al. 2019, ApJ, 882, 8
Savorgnan, G. A. D., & Graham, A. W. 2016, ApJS, 222, 10
Schawinski, K., Dowlin, N., Thomas, D., Urry, C. M., & Edmondson, E. 2010,
     JL, 714, L108
Schaye, J., Aguirre, A., Kim, T.-S., et al. 2003, ApJ, 596, 768
Schaye, J., Crain, R. A., Bower, R. G., et al. 2015, MNRAS, 446, 521
Schleicher, D. R. G., Palla, F., Ferrara, A., Galli, D., & Latif, M. 2013, A&A,
Sharma, R. S., Brooks, A. M., Somerville, R. S., et al. 2020, ApJ, 897, 103
Sharma, R. S., Brooks, A. M., Tremmel, M., Bellovary, J., & Quinn, T. R.
  2022, ApJ, 936, 82
Shen, J., Vanden Berk, D. E., Schneider, D. P., & Hall, P. B. 2008, AJ,
  135, 928
Shen, S., Madau, P., Aguirre, A., et al. 2012, ApJ, 760, 50
Shen, S., Wadsley, J., & Stinson, G. 2010, MNRAS, 407, 1581
Stinson, G., Seth, A., Katz, N., et al. 2006, MNRAS, 373, 1074
Stinson, G. S., Brook, C., Prochaska, J. X., et al. 2012, MNRAS, 425, 1270
Suresh, J., Rubin, K. H. R., Kannan, R., et al. 2017, MNRAS, 465, 2966
Telford, O. G., Werk, J. K., Dalcanton, J. J., & Williams, B. F. 2019, ApJ,
  877, 120
Tremmel, M., Governato, F., Volonteri, M., & Quinn, T. R. 2015, MNRAS,
  451, 1868
Tremmel, M., Karcher, M., Governato, F., et al. 2017, MNRAS, 470, 1121
Tremmel, M., Quinn, T. R., Ricarte, A., et al. 2019, MNRAS, 483, 3336
Tremonti, C. A., Heckman, T. M., Kauffmann, G., et al. 2004, ApJ, 613, 898
Tripp, T. M., Meiring, J. D., Prochaska, J. X., et al. 2011, Sci, 334, 952
Tsujimoto, T., Nomoto, K., Yoshii, Y., et al. 1995, MNRAS, 277, 945
Tumlinson, J., Thom, C., Werk, J. K., et al. 2013, ApJ, 777, 59
Van Den Bosch, F. C., Yang, X., Mo, H. J., et al. 2007, MNRAS, 376, 841
van de Voort, F., Schaye, J., Booth, C. M., Haas, M. R., & Dalla Vecchia, C.
  2011, MNR
               S, 414, 2458
Vincenzo, F., Matteucci, F., Belfiore, F., & Maiolino, R. 2016, MNRAS,
  455, 4183
Vogelsberger, M., Genel, S., Springel, V., et al. 2014, MNRAS, 444, 1518
Volonteri, M. 2012, Sci, 337, 544
Volonteri, M., & Natarajan, P. 2009, MNRAS, 400, 1911
Wadsley, J., Stadel, J., & Quinn, T. 2004, NewA, 9, 137
Wadsley, J. W., Keller, B. W., & Quinn, T. R. 2017, MNRAS, 471, 2357
Wadsley, J. W., Veeravalli, G., & Couchman, H. M. P. 2008, MNRAS,
Weinberger, R., Springel, V., Hernquist, L., et al. 2017, MNRAS, 465, 3291
Wellons, S., Faucher-Giguère, C.-A., Hopkins, P. F., et al. 2023, MNRAS,
  520, 5394
Werk, J. K., Bentz, M. C., Burchett, J. N., et al. 2021, HST Proposal, 16650
Werk, J. K., Prochaska, J. X., Thom, C., et al. 2013, ApJS, 204, 17
Whitmore, B. C. 1980, ApJ, 242, 53
Wilde, M. C., Werk, J. K., Burchett, J. N., et al. 2021, ApJ, 912, 9
Zahid, H. J., Sohn, J., & Geller, M. J. 2018, ApJ, 859, 96
Zou, H., Yang, Y. B., Zhang, T. M., et al. 2011, RAA, 11, 1093
```